HHS Public Access

Author manuscript

J Am Chem Soc. Author manuscript; available in PMC 2018 August 02.

Published in final edited form as:

J Am Chem Soc. 2017 August 02; 139(30): 10472–10485. doi:10.1021/jacs.7b05389.

Unprecedented (μ-1,1-Peroxo)diferric Structure for the Ambiphilic Orange Peroxo Intermediate of the Nonheme *N*-Oxygenase CmlI

Andrew J. Jasniewski[†,‡,#], **Anna J. Komor**[†,‡,#], **John D. Lipscomb**[‡,§,*], and **Lawrence Que Jr**[†,‡,*]

[†]Department of Chemistry, University of Minnesota, Minneapolis, Minnesota 55455

[§]Department of Biochemistry, Molecular Biology, and Biophysics, University of Minnesota, Minneapolis, Minnesota 55455

[‡]Center for Metals in Biocatalysis, University of Minnesota, Minneapolis, Minnesota 55455

Abstract

The final step in the biosynthesis of the antibiotic chloramphenicol is the oxidation of an aryl-amine substrate to an aryl-nitro product catalyzed by the *N*-oxygenase CmlI in three two-electron steps. The CmlI active site contains a diiron cluster ligated by three histidine and four glutamate residues, and activates dioxygen to perform its role in the biosynthetic pathway. It was previously shown that the active oxidant used by CmlI to facilitate this chemistry is a peroxo-diferric intermediate (**CmlI^{P}**). Spectroscopic characterization demonstrated that the peroxo binding geometry of **CmlI^{P}** is not consistent with the μ-1,2 mode commonly observed in nonheme diiron systems. Its geometry was tentatively assigned as μ-η^2:η^1 based on comparison with resonance Raman (rR) features of mixed-metal model complexes in the absence of appropriate diiron models. Here, X-ray absorption spectroscopy (XAS) and rR studies have been used to establish a refined structure for the diferric cluster of **CmlI^{P}**. The rR experiments carried out with isotopically labeled water identified the symmetric and asymmetric vibrations of an Fe–O–Fe unit in the active site at 485 and 780 cm^{-1}, respectively, which was confirmed by the 1.83-Å Fe–O bond observed by XAS. In addition, a unique Fe•••O scatterer at 2.82 Å observed from XAS analysis is assigned as arising from the distal O atom of a μ-1,1-peroxo ligand that is bound symmetrically between the irons. The (μ-oxo)(μ-1,1-peroxo)diferric core structure associated with **CmlI^{P}** is unprecedented among diiron cluster-containing enzymes and corresponding biomimetic complexes. Importantly, it allows the peroxo-diferric intermediate to be ambiphilic, acting as an electrophilic oxidant in the initial *N*-hydroxylation of an arylamine and then becoming a nucleophilic oxidant in the final oxidation of an aryl-nitroso intermediate to the aryl-nitro product.

[*]Corresponding Authors: lipsc001@umn.edu, larryque@umn.edu.
[#]Contributed equally to the study.
Current addresses: Department of Molecular Biology and Biochemistry, University of California Irvine, Irvine, CA 92697 United States (AJJ) and Leibniz Institute for Natural Product Research and Infection Biology, Jena, Germany (AJK).

The authors declare no competing financial interest.

Supporting Information

The Supporting Information is available free of charge on the ACS Publications website at DOI: XANES and EXAFS analysis with fit parameters and full resonance Raman spectra for **CmlI^{R}**, **CmlI^{Ox}**, and **CmlI^{P}**

Graphical Abstract

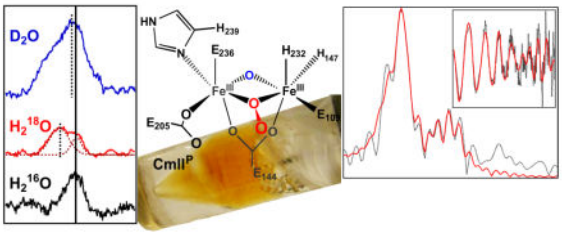

Keywords

X-ray absorption spectroscopy; Raman spectroscopy; Non-heme iron; Diiron cluster; Oxygen activation; Nonribosomal peptide synthetase

Introduction

Nonheme diiron enzymes are capable of facilitating a variety of difficult chemical transformations *via* oxygen activation, including C–H bond hydroxylation, C–C bond desaturation, the generation of alkanes from aldehydes, and *N*-oxygenation of aryl amine substrates, among others.[1–8] The diiron cluster-containing *N*-oxygenase CmlI is a member of this latter class. It serves as a tailoring enzyme on the non-ribosomal peptide synthetase biosynthetic pathway that is responsible for producing the antibiotic chloramphenicol in the soil bacterium *Streptomyces venezuelae*.[9–14] CmlI catalyzes a six-electron oxidation of the aryl-amine precursor to form the aryl-nitro group of the active antibiotic (Figure 1).

Characterization of the aryl-amine conversion by CmlI has provided the strongest evidence to date for the involvement of a new type of oxidant in diiron-cluster-mediated oxygenation reactions.[15] The canonical scheme for dioxygen activation by diiron-cluster-containing enzymes is based on the well-studied diiron enzyme soluble methane monooxygenase (sMMOH). Dioxygen binds to the diferrous form of the enzyme to generate a peroxo-diferric intermediate (**P**), which then undergoes O–O bond cleavage to generate a high-valent bis(μ-oxo)diiron(IV) cluster (**Q**). **Q** is the reactive intermediate responsible for C–H bond activation in the sMMOH catalytic cycle. Another canonical diiron enzyme, ribonucleotide reductase (RNR) from *E. coli*, uses a diiron center in its R2 subunit, to activate O_2 and generate a functionally essential tyrosyl radical. This oxidation is carried out by a high-valent oxidant called **X** with a (μ-oxo)iron(III)iron(IV) core.[16–18] sMMOH and RNR are the only enzymes with diiron active sites for which high-valent iron oxidants have been identified, but such oxidants have been postulated to be the reactive intermediate formed in most diiron oxygenases.

Diferric-peroxo (**P**) species have been trapped and characterized in the reactions of O_2 with the diferrous forms of the classical diiron oxygen activating enzymes, sMMOH,[19–21] RNR R2,[22–24] and stearoyl-CoA Δ^9-desaturase (Δ^9D),[25] but their functions in their respective catalytic cycles have generally been to act as a precursor to the high-valent active oxidant. Analysis of these **P** intermediates has suggested that diiron-peroxo species generally adopt a

cis-μ-1,2-peroxo binding mode (Figure 2) and that **P** intermediates are not the actual oxidants on the native catalytic cycles, except in rare cases of easily oxidized substrates.[26–27] These assumptions are bolstered by the availability of several synthetic (μ-1,2-peroxo)diferric complexes for which the X-ray crystal structures are known.[28–32] These complexes, supported by ligands with N- and O-donors to mimic the histidine/carboxylate active sites of the enzymes have been well characterized by various spectroscopic methods to provide a set of parameters to which enzymatic **P** species can be compared. However, these synthetic peroxo complexes are fairly stable and generally unreactive, and therefore do not provide much insight into the mechanism of oxidation by a **P** species.

The first reactive **P** intermediate was discovered in 2005 by Lippard and co-workers,[26] when they demonstrated that the **P** species of sMMOH directly reacts with ether and alcohol substrates. However, definitive structural characterization of this **P** intermediate is unavailable. In 2009, a hyperstable ($t_{1/2}$ > 24 hrs at room temperature) (μ-hydroxo)(*cis*-μ-1,2-peroxo)diferric intermediate was discovered and characterized[33] from the human enzyme deoxyhypusine hydroxylase (hDOHH) that decays concomitant with the formation of the native hydroxylated product, demonstrating that stable *cis*-μ-1,2-peroxo species can be activated.[33] In 2013, a peroxo-diferric species was reported for the cyanobacterial aldehyde deformylating oxygenase (cADO) and proposed to function as a nucleophilic oxidant for the aldehyde substrate.[34] A final set of examples comes from the related enzymes toluene-4-monooxygenase (T4MO) and toluene/o-xylene monooxygenase (ToMO), which fall into the diiron oxygenase subclass bacterial multicomponent monooxygenases with sMMOH. A recent crystal structure from T4MO was obtained of an arylperoxo species bound in a μ-η^2:η^2 configuration to the diiron cluster (T4MO$^{\mathbf{P}}$$\eta^2$),[35] which was shown *in crystallo* to be an intermediate for the hydroxylation of toluene. The putative **P** intermediate of ToMO (ToMO$^{\mathbf{P}}$) from the wild type enzyme is a short-lived ($t_{1/2}$ ~ 15 s) diferric species that appears to be active towards arene substrates, but can only be characterized by Mössbauer spectroscopy, and has no accompanying visible chromophore.[36] Its Mössbauer parameters significantly differ from those observed for the **P** from sMMOH and other *cis* μ-1,2-peroxo-diferric intermediates, and its structure remains unknown. An inactive **P** intermediate has also been generated from the T201S mutant of ToMO, with spectroscopic signatures that match those of sMMOH.[37] These examples provide evidence that diferric-peroxo species can serve as the active oxidant instead of a high-valent intermediate such as **Q** or **X** for some types of substrates.

In the past, geometric assignments of enzymatic **P** intermediates have been largely based on the comparison of their spectroscopic parameters to those of structurally characterized synthetic **P** analogs. Recently, the X-ray crystal structures of enzymatic **P** intermediates have been determined for hDOHH,[38] a truncated CmlI (**CmlIΔ33**),[39] and T4MO.[35, 40] The hDOHH crystal structure confirms the *cis*-μ-1,2-peroxo binding mode earlier assigned by resonance Raman studies, although the Fe•••Fe distance in the crystallized hDOHH suggests that this enzyme may have suffered from photoreduction by the X-ray beam, which is a well known issue in metalloenzyme crystallography.[41–43] Therefore, the specific distances should be viewed with some skepticism. The crystallized **CmlIΔ33**$^{\mathbf{P}}$ also shows a *cis*-μ-1,2-peroxo

binding mode, but the species does not react with substrate, nor does it have the same UV-vis absorption spectrum as the known active **P**. Consequently, this crystallized CmlI-peroxo species is thought not to represent the active or native peroxo intermediate. Two different reactive peroxo species have been crystallized from the T4MO system, with different peroxo binding modes. A *cis*-μ-1,2-peroxo intermediate (T4MO$^{\mathbf{P}}$) is prepared by soaking crystals of diferric T4MO with H_2O_2. Accordingly, T4MO is active *via* the peroxide shunt as first described for sMMOH,[40, 44] though the reaction is ~600 times slower than that carried out with the native biological reductants and O_2. The more recent crystal structure reveals a μ-η^2: η^2-arylperoxo intermediate (T4MO$^{\mathbf{P}\eta^2}$), prepared by soaking crystals of diferrous T4MO with toluene and then exposing them to O_2. T4MO $^{\mathbf{P}\eta^2}$ is proposed to be part of the native reaction cycle. Of the three crystallized enzymatic μ-1,2-peroxo **P** species, only hDOHH$^{\mathbf{P}}$ is shown to be active in the native cycle. The high stability and low reactivity of many of the *cis*-μ-1,2 **P** species (synthetic and enzymatic) suggest that this geometry may not be the active species. However, the new evidence implicating enzymatic **P** species, like T4MO$^{\mathbf{P}\eta^2}$, as the active oxidant in some enzyme cycles emphasizes the notion that alternative types of peroxo intermediates with much higher reactivity can exist.

In 2015, we published the first evidence for a distinct **P** species from CmlI.[8] Kinetic studies showed that **CmlI$^{\mathbf{P}}$** reacts rapidly with substrates to yield oxygenated products. However, it is unusually stable in the absence of substrate, exhibiting a half-life of ~3 h at 4 ºC. This long lifetime allowed some of the spectroscopic features of **CmlI$^{\mathbf{P}}$** to be determined in detail, revealing that it is distinct from all but one of the previously reported peroxo intermediates. The *N*-oxygenase AurF was found to have a **P** species (AurF$^{\mathbf{P}}$) with similar electronic absorption maximum and Mössbauer parameters as **CmlI$^{\mathbf{P}}$**, but the half-life of AurF$^{\mathbf{P}}$ is much shorter (~7 min at 4 ºC), and structural characterization is unavailable.[45] In contrast to the typical *cis*-μ-1,2-peroxo species with absorbance maxima near 700 nm, **CmlI$^{\mathbf{P}}$** and AurF$^{\mathbf{P}}$ instead have significant absorption at 500 nm. Resonance Raman (rR) experiments of **CmlI$^{\mathbf{P}}$** showed a ν(O–O) at 791 cm^{-1} that was definitively assigned using $^{18}O_2$ and $^{16}O^{18}O$ labeling experiments.[8] The ν(O–O) of **CmlI$^{\mathbf{P}}$** is much lower in frequency than that of any known biological or synthetic diiron-cluster **P** species. The commonly observed (μ-1,2-peroxo)diferric species generally exhibit a range of 840 – 925 cm^{-1} for the ν(O–O) feature. Mössbauer analysis showed that **CmlI$^{\mathbf{P}}$** has two inequivalent Fe centers, while (μ-1,2-peroxo)-diferric species generally have two similar iron(III) sites.[8] Unfortunately, there were no diiron peroxo model complexes available to allow a definitive structural assignment based on this spectroscopic data. Consequently, the **CmlI$^{\mathbf{P}}$** peroxo structure was suggested to be μ-η^1: η^2 based on the similarity of its rR parameters to those of mixed-metal peroxo complexes that have comparably low ν(O–O) frequencies.[46–49]

We have recently proposed that chloramphenicol is synthesized in three 2-electron oxidation steps from its arylamine precursor as illustrated in Scheme 1.[15] **CmlI$^{\mathbf{P}}$** carries out both the arylamine-to-arylhydroxylamine and the arylnitroso-to-arylnitro steps in which the oxygen transfer reactions occur. The intervening arylhydroxylamine-to-arylnitroso step is thought to be an internal redox process in the active site of CmlI that results in diiron cluster reduction to allow re-formation of **CmlI$^{\mathbf{P}}$** to be used in the final step of chloramphenicol synthesis. The substrates for each of the three oxidation steps in this biosynthetic pathway differ

substantially in their electronic nature, requiring that **CmlI^{P}** be able to react with both electron-rich and electron-poor substrates, a quality we have termed ambiphilic reactivity.

In the current study, we have used X-ray absorption spectroscopy (XAS) and rR spectroscopy to structurally characterize three different states of CmlI, including **CmlI^{P}**. A new view of the structure is now presented based on this spectroscopic investigation. Our studies further refine the active site picture for **CmlI^{P}**, identifying the diiron core as having both an oxo and a μ-1,1-peroxo bridge. This novel diiron peroxo core structure sheds some light on the ambiphilic reactivity of the diiron cluster of CmlI and supports the notion that these are reactive peroxo intermediates that function within the canonical diiron framework.

EXPERIMENTAL PROCEDURES

Overexpression and Purification of CmlI

Expression of CmlI was performed in *E. coli* BL21(DE3) in M9 minimal medium in the presence of 100 μg/ml ampicillin. A His-tagged construct described previously was used.[8] Cells were grown to an OD ~ 1.0 and induced with 150 μM isopropyl-β-D-1-thiogalactopyranoside (IPTG) and 50 μM $FeCl_3$ at which point the temperature was lowered to 20 °C and grown for an additional 15 h. Cells were harvested by centrifugation and stored at −80 °C until further use. Cells were resuspended in 50 mM potassium phosphate pH 7.4, 300 mM NaCl, 10 mM imidazole, lysed via sonication, and centrifuged. The resulting supernatant was loaded onto a Ni nitrilotriacetic acid column (Qiagen) equilibrated in the same buffer. After loading, the column was washed with the above buffer containing 20 mM imidazole, and protein was eluted in the same buffer containing 300 mM imidazole. Protein-containing fractions were pooled and dialyzed against 50 mM Bicine pH 9 and stored at −80 °C until further use. CmlI concentrations were determined by the calculated extinction coefficient (ε_{280} = 50 mM^{-1} cm^{-1}).

CmlI^{Ox} Sample

As-isolated CmlI (**CmlI^{Ox}**) was thawed and concentrated to 3–4 mM by centrifugal filtration (Amicon Ultra-0.5 mL centrifugal filters, kDa 10 cutoff), and then mixed with glycerol to a final concentration of ~20% v/v. After loading into an XAS cup, the sample was flash frozen with LN_2. For the generation of D_2O samples (**CmlI^{Ox}-D$_2$O**), a minimum of 5 concentration and re-dilution cycles was used to exchange into 50 mM Bicine pD 9 prepared with D_2O. No glycerol was used in D_2O-containing samples.

Generation of CmlI^{R} and CmlI^{P} Samples for XAS

An aliquot of CmlI was degassed on an Ar Schlenk line and then brought into an anaerobic chamber where the reductant sodium hydrosulfite (10x molar excess) and the reduction mediator methyl viologen (20 μM final concentration) were added to the protein. The protein was stirred for 35 min to ensure the blue color from the methyl viologen remained, indicating complete reduction. The sodium hydrosulfite and methyl viologen were then removed by passing the CmlI through a PD-10 size exclusion column equilibrated with 50 mM Bicine, pH 9. Several fractions were collected and concentrated to 3–4 mM enzyme

anaerobically using a centrifuge located within the anaerobic chamber and spin filters as described above.

Reduced—While in the anaerobic chamber, 400 μl of reduced enzyme was mixed with 100 μl glycerol and then loaded into an XAS cup (**CmlI^{R}**). The cup was then sealed in a large Reacti-Vial (Thermo Scientific). The vial was brought out of the chamber and submerged in LN_2. Only after the sample was frozen was the vial opened and the sample stored under LN_2.

Peroxo—A reduced sample was removed from the anaerobic chamber in a Reacti-Vial and then the peroxo intermediate was generated by blowing pure O_2 over the surface of the sample while stirring vigorously for 3 min. Glycerol was added to final concentration of ~20% by volume, and then the solution was placed in an XAS cup and frozen in LN_2. All work outside of the anaerobic chamber was done on ice and/or in a 4 °C cold room.

Generation of CmlI^{Ox} and CmlI^{P} Samples for rR. CmlI^{Ox} and CmlI^{P} samples for rR were prepared in the same manner as the corresponding XAS samples, except that samples were loaded into flat-bottomed NMR tubes and were kept frozen until they were analyzed.

D_2O—CmlI^{P} in D_2O (**CmlI^{P}-D_2O**) was generated as described above, except that after the reduction step the enzyme was passed through a PD-10 size exclusion column equilibrated with buffer prepared with D_2O (50 mM Bicine, pD 9). Concentration and re-dilution with D_2O buffer a minimum of two times, interspersed with 30 minute incubation periods, ensured nearly complete isotope exchange. Samples prepared with D_2O did not contain glycerol.

$^{18}OH_2$—CmlI^{P} and **CmlI^{Ox}** in $^{18}OH_2$ were prepared in the same manner as their corresponding standard water samples, with the addition of several concentration and dilution cycles and 30 minute incubation periods to exchange the $^{16}OH_2$-containing buffer with the $^{18}OH_2$-containing buffer. In the **CmlI^{P}** preparation, the exchange was performed on the diferrous enzyme in an anaerobic chamber. To prepare $^{18}OH_2$-containing buffer, 2 mL of standard buffer (50 mM Bicine, pH 9) was lyophilized for 24 h. The resulting salts were then dissolved in 2 ml $^{18}OH_2$ water, either anaerobically or on the bench top, as required by the sample.

X-ray Absorption Spectroscopy

Iron K-edge X-ray absorption spectra were collected on SSRL beam line 7–3 and 9-3 using a 30 element and 100 element (respectively) solid state Ge detector (Canberra) with a SPEAR storage ring current of ~500 mA at a power of 3.0 GeV. The incoming X-rays were unfocused using a Si(220) double crystal monochromator, which was detuned to 40% of the maximal flux to attenuate harmonic X-rays. For **CmlI^{R}** and **CmlI^{Ox}**, 16 and 12 scans, respectively, were collected. For **CmlI^{P}**, two samples with 9 and 10 scans were collected and averaged. All scans were between 6882 eV and 8000 eV at ~10 K using an Oxford Instruments CF1208 continuous flow liquid helium cryostat. An iron foil was placed in the beam pathway prior to the ionization chamber I_0 and scanned concomitantly for an energy

calibration, with the first inflection point of the edge assigned to 7112.0 eV. A 3 μm Mn filter was used for the collection of **CmlI^{R}** and **CmlI^{Ox}**, and a "9" μm Mn filter (3 μm + 6 μm) and a Soller slit were used to increase the signal to noise ratio of the spectra for **CmlI^{P}**. Photoreduction was monitored by scanning the same spot on the sample twice and comparing the first derivative peaks associated with the edge energy during collection.

The detector channels from the scans were examined, calibrated, averaged, and processed for EXAFS analysis using EXAFSPAK[50] to extract X(k). Theoretical phase and amplitude parameters for a given absorber-scatterer pair were calculated using FEFF 8.40[51] and were utilized by the "opt" program of the EXAFSPAK package during curve fitting. Parameters for each species were calculated using a model derived from the crystal structure of analogous enzyme AurF (PDB code 3CHH). In all analyses, the coordination number of a given shell was a fixed parameter and was varied iteratively in integer steps, while the bond lengths (R) and mean-square deviation (σ^2) were allowed to freely float. The amplitude reduction factor S_0 was fixed at 0.9, while the edge-shift parameters E_0 was allowed to float as a single value for all shells. Thus, in any given fit, the number of floating parameters was typically equal to (2 x num shells) + 1. **CmlI^{R}** has a k range of 2 – 14 Å^{-1} and **CmlI^{Ox}** and **CmlI^{P}** have a range of 2 – 15 Å^{-1}.

Pre-edge analysis was performed on data normalized in the "process" program of the EXAFSPAK package, and pre-edge features were fit as described elsewhere[52] between 7108 eV to 7118 eV using the Fityk[53] program with pseudo-Voigt functions composed of 50:50 Gaussian/Lorentzian functions.

Resonance Raman Spectroscopy

Resonance Raman spectra were obtained at ~4 ºC with excitation at 561 nm (100 mW at source, Cobolt Jive 04-01 series) through the sample in a flat bottom NMR tube using a 90° backscattering arrangement (parallel to the slit direction). The collimated Raman scattering was collected using two Plano convex lenses (f = 12 cm, placed at an appropriate distance) through the appropriate long pass edge filter (Semrock) into an Acton AM-506M3 monochromator equipped with a Princeton Instruments ACTON PyLON LN/ CCD-1340x400 detector. The detector was cooled to −120 °C prior to the experiments. Spectral calibration was performed using the Raman spectrum of acetonitrile/toluene 50:50 (v:v). The spectra of **CmlI^{Ox}** were collected with 180, 450 and 225 scans with acquisition times of 5s, 2s and 4s for the ^{16}O, ^{18}O and D_2O samples, respectively, for a total of 15 min collections. The spectra of **CmlI^{P}** were collected with 180 scans with an acquisition time of 10s for the ^{18} O and D_2O samples for a total of 30 min collections, and 225 scans with an acquisition time of 4s for the ^{16}O samples for a total of 15 min. The collected data was processed using Spekwin32,[54] and a multipoint baseline correction was performed for all spectra.

RESULTS

X-ray absorption near edge structure (XANES) analysis was utilized to gain structural insight into the active sites of three CmlI species: **CmlI^{R}**, **CmlI^{Ox}**, and **CmlI^{P}** (Figure 3). This analysis provides information about the oxidation state (from the Fe K-edge energy)

and the symmetry (from the pre-edge peak area) of the target metal centers. The K-edge energy for **CmlI^{R}** is 7122.1 eV, which falls in the range typical for diferrous species (7121 eV – 7123 eV).[55–58] **CmlI^{Ox}** has a K-edge energy of 7124.1 eV, which is two electron volts higher than that of the reduced species. This difference in K-edge energy is consistent with the difference observed between diferrous and diferric states in other diiron enzyme systems (Table 1).[57–59] The oxygenated **CmlI^{P}** has a K-edge of 7124.9 eV, which falls lower than found for hDOHH^{P} (7125.6 eV)[57] but within the range found for synthetic (μ-1,2-peroxo)diferric complexes having an additional single-atom bridge (7123 – 7126 eV).[60–63]

The pre-edge peak in the XANES region corresponds to a formally forbidden 1s → 3d transition in first row transition metal complexes.[64] The intensity of the pre-edge peak increases as the metal center is distorted away from centrosymmetry, which is reflected in a larger pre-edge peak area.[65]. The fits of the pre-edge features are summarized in Table 1 and individual fits of the pre-edge region are shown in Figures S1 – S3. The pre-edge feature of **CmlI^{R}** is fit with pseudo-Voigt functions that yield an area of 8.4 units, which falls between values for five-coordinate (~11 units) and six-coordinate (~5 units) diferrous centers,[66] and is similar to the recently reported value for six-coordinate diferrous CmlA.[58] The pre-edge area of **CmlI^{Ox}** is 14.5 units, consistent with a six-coordinate (μ-oxo)diferric center (ave, 14.5 units).[52, 67] Interestingly, **CmlI^{P}** has a pre-edge area of 19.2 units, which is significantly higher than that of hDOHH^{P} (12.4 units)[57] and those found for synthetic six-coordinate diferric-peroxo complexes (13 – 16 units).[60–61, 63] As synthetic (μ-oxo)diferric complexes with two five-coordinate centers have been reported to have pre-edge areas of ~24 units,[67] averaging the contributions of one six-coordinate Fe center and one five-coordinate Fe center would give rise a pre-edge area of 19.3 units, so the value of 19.2 units obtained for **CmlI^{P}** would be consistent with the presence of such a diferric complex.

Extended X-ray absorption fine structure (EXAFS) analysis provides information about the nature of the ligands to the iron centers and the Fe•••Fe distance. Key features of the best fits for each species are listed in Table 2, and the fitting protocols that led to the best fits for individual species can be found in the supplementary information (Figures S5 – S6, Tables S1 – S3). The Fourier transformed (FT) EXAFS data of the various CmlI samples all show an intense feature at R + Δ < 2 Å that is assigned to the scattering atoms of the primary coordination sphere, while the weaker features observed at R + Δ > 2 Å are generally associated with outer sphere interactions such as the other Fe atom in the dinuclear active site as well as the C/N atoms from His residues and carboxylates, as observed in the EXAFS analysis of other nonheme diiron enzymes.[18, 57–58, 68–69]

The first coordination sphere of **CmlI^{R}** consists of 1 Fe–O/N at 1.94 Å and 5 Fe–N/O scatterers at 2.10 Å (Table 2). The scatterers at 2.10 Å arise from protein-derived carboxylate and histidine ligands, as we have established previously for hDOHH and CmlA.[57–58] These assignments are based on metal-ligand distances found in the crystal structures of nonheme diiron proteins,[7, 70–77] including diferrous CmlI.[39] The shorter Fe–N/O distance at 1.94 Å is assigned to a μ-hydroxo bridge based on comparison to the Fe–O distances associated with the μ-hydroxo ligand in the reduced clusters of CmlA[58] and synthetic (μ-hydroxo)diferrous complexes.[78–80]

Beyond the primary sphere, the fits provide evidence for a low-Z scatterer at 2.58 Å and an Fe scatterer at 3.35 Å. The distance associated with the former and its small Debye-Waller factor (σ^2) are consistent with the carbon atom from a bidentately bound carboxylate ligand.[58–59, 70] The fact that N = 1 for this scatterer indicates that there must be an average of one bidentate carboxylate per Fe in **CmlI^{R}**. Also observed is an Fe scatterer at 3.35 Å with a σ^2 of 9.90×10^{-3} Å^2. This relatively high value suggests a greater variance in the Fe•••Fe distance that likely reflects fairly flexible Fe(II)–μ-O(H/R) bonds. Indeed, similarly large σ^2 values have been reported for other reduced diiron enzymes such as Fe(II)Fe(III)-uteroferrin (12×10^{-3} Å^2) and Fe(II)Fe(II)-sMMOH (13.3×10^{-3} Å^2).[68, 81] The active site picture thus obtained for **CmlI^{R}** in frozen solution from EXAFS analysis differs significantly from that derived from the crystal structure of **CmlI 33^{R}**.[39] For the latter, the hydroxo bridge observed in the EXAFS analysis is absent. Instead, there is a bidentate carboxylate bridge (E326) that gives rise to a longer Fe•••Fe distance of 3.6 Å. For reasons that are described in detail in the Discussion, we believe that the EXAFS results better model the active conformation of the enzyme.

The best fit to the EXAFS data for diferric **CmlI^{Ox}** yields three shells of scatterers of the first coordination sphere, with one Fe–O/N at 1.83 Å, two Fe–O/N at 2.00 Å, and three Fe–N/O at 2.15 Å (Table 2). The much shorter Fe–O distance at 1.83 Å corresponds to a μ-oxo bridge that forms by loss of the proton from the μ-hydroxo bridge of **CmlI^{R}** upon oxidation to **CmlI^{Ox}**. The assignment of an oxo bridge at 1.83 Å would also be consistent with the large pre-edge area associated with **CmlI^{Ox}** presented earlier. The main component of the first coordination sphere associated with 5 N/O scatterers in **CmlI^{R}** becomes resolved in **CmlI^{Ox}** into two subshells at 2.00 and 2.15 Å with small σ^2 values. Unlike for **CmlI^{R}**, the fit for **CmlI^{Ox}** does not require a carbon scatterer at ~2.6 Å, suggesting that the bidentate carboxylate ligands found in **CmlI^{R}** have become monodentate. Notably, the Fe•••Fe distance at 3.32 Å for **CmlI^{Ox}** remains essentially the same as that found for the reduced enzyme, a phenomenon that has also been observed for CmlA and hDOHH.[57–58]

The best fit for **CmlI^{P}** is similar to that of **CmlI^{Ox}** except for the inclusion of a scatterer at 2.82 Å (Table 2). The major FT peak at R + Δ ~ 1.7 Å (Figure 4, top left) corresponds to one Fe–O/N at 1.83 Å, two Fe–O/N at 1.98 Å, and three Fe–N/O at 2.13 Å. The assignments of these distances correspond to those for **CmlI^{Ox}**, including the 1.83-Å oxygen scatterer as a μ-oxo bridge. The only difference is that one of the scatterers at 1.98 Å for **CmlI^{P}** is now assigned to the proximal oxygen atom of the peroxo moiety. The Fe•••Fe distance is 3.35 Å, essentially unchanged within error relative to those observed for **CmlI^{Ox}** and **CmlI^{R}**.

The most notable feature of the **CmlI^{P}** fit is the requirement for a Fe•••O scatterer at 2.82 Å, as demonstrated by the better fit of the FT peaks centered at ~ 2.5 Å (Figure 4, compare middle to bottom) as well as the increase in the goodness-of-fit value upon deletion of this scatterer (see Table S3, fit 23 versus fit 26). This scatterer is not required in the fits for **CmlI^{Ox}**, **CmlI^{R}** or decayed **CmlI^{P}** samples and is therefore unique to, and diagnostic of, **CmlI^{P}**. The 2.82-Å scatterer has a σ^2 value of 1.50×10^{-3} Å^2, which is remarkably low for a low-Z scatterer beyond the first coordination sphere, implying that this scatterer is held relatively well fixed in space. In addition, it must also be positioned equidistant to the two Fe centers; otherwise, a higher σ^2 value should be observed to reflect the different Fe1–O and

Fe2–O distances. Reducing the N value for this scatterer to 0.5 to reflect a model in which this scatterer is only 2.82 Å away from one of the two Fe's in the active site results in an unacceptable negative σ^2 value of -1.50×10^{-3} Å^2 (Table S3, fit 29). This fit further supports the assignment of a 2.82-Å scatterer that is equidistant from both Fe centers. As such a scatterer has not been found thus far in the EXAFS analysis of any other diferric-peroxo species, its presence suggests that the peroxo ligand of **CmlI^{P}** must not be bound in the usual μ-1,2 mode, in line with its unusually low ν(O–O) frequency of 791 cm^{-1}.[8]

Resonance Raman Characterization of CmlI^{Ox} and CmlI^{P}

Resonance Raman experiments performed on **CmlI^{Ox}** and **CmlI^{P}** confirm the presence of the μ-oxo ligand identified in the EXAFS analysis (see Figure S7 for full spectra). The rR spectrum of **CmlI^{Ox}** obtained in $^{16}OH_2$ shows a peak at 487 cm^{-1} (Figure 5, left panel), which downshifts 18 cm^{-1} to 469 cm^{-1} in a sample of **CmlI^{Ox}** prepared in $^{18}OH_2$ (Figure 5, middle panel). Both the location of the peak and the magnitude of the shift are consistent with its assignment to ν_s(Fe-O-Fe), the symmetric Fe–O–Fe stretching mode of a (μ-oxo)diferric center. For comparison, the ν_s(Fe–O–Fe) vibrational mode for the (μ-oxo)diferric center in CmlA was observed at a similar value of 481 cm^{-1} with a ^{18}O downshift of 17 cm^{-1}.[59]

To put this vibration into a broader context, we compared its frequency with data originally collected by Sanders-Loehr and co-workers on a large number of (μ-oxo)diferric complexes, which established a correlation between ν(Fe–O–Fe) and ∠Fe–O–Fe values.[82] Since the original 1989 study, examples of oxo-bridged diiron complexes with an additional μ-1,2-peroxo bridge (green squares) have been characterized,[32, 60–62, 83] as well as complexes with bis(μ-oxo)diiron diamond cores.[84–86] These new data have been included to the plot shown in Figure 6 and extend the correlation to entries with Fe–O–Fe angles approaching 90°. Based on Figure 6, the observed ν_s(Fe–O–Fe) frequency of 487 cm^{-1} would then correspond to an ∠Fe–O–Fe of ~134° for the Fe–O–Fe unit in **CmlI^{Ox}**, which is in good agreement with an angle of 130° that is calculated assuming Fe1–O and Fe2–O distances of 1.83 Å and an Fe•••Fe distance of 3.32 Å.

Close inspection of the 740–800-cm^{-1} region in the $^{16}OH_2$ and $^{18}OH_2$ samples of **CmlI^{Ox}** shows the loss of signal intensity at ~780 cm^{-1} when the $^{16}OH_2$ buffer solution is replaced by $^{18}OH_2$, unmasking a peak at ~790 cm^{-1} that is assigned to protein-related vibration (Figure 7, left top and left middle). Fitting the protein-related features with Gaussian functions did not sufficiently fit the peaks in the Raman spectrum. In the $^{16}OH_2$ sample an additional function centered at 780 cm^{-1} was required, while functions at 780 cm^{-1} and 750 cm^{-1} had to be included in the $^{18}OH_2$ sample, which are consistent with their respective assignments to ν_{as}(Fe–O–Fe) modes of the ^{16}O and ^{18}O isotopomers. Based on the correlation shown in Figure 6, they correspond to an ∠Fe–O–Fe of 138º, which is in agreement with the EXAFS-derived angle of 135º for **CmlI^{Ox}**.

Raman data also confirm the retention of the oxo bridge in **CmlI^{P}**. Examination of the 500-cm^{-1} region of **CmlI^{P}** reveals a peak at 485 cm^{-1}, which downshifts to 467 cm^{-1} in $^{18}OH_2$ buffer (Figure 5, center) and can be assigned to ν_s(Fe–O–Fe). The similar frequencies of this feature in both **CmlI^{Ox}** and **CmlI^{P}** suggest little difference between the Fe–O–Fe angles of

CmlI^{Ox} and **CmlI^{P}**, in agreement with the EXAFS analysis. The corresponding ν_{as}(Fe–O–Fe) mode is found to be in the same region as a protein-derived mode at 758 cm^{-1} and the previously identified ν_{s}(O–O) vibration at 791 cm^{-1} (789 cm^{-1} in the present study). Fitting the 740–800 cm^{-1} region of the $^{16}OH_2$ sample only with Gaussian functions at 758 cm^{-1} and 789 cm^{-1} is insufficient to match the observed peak shape and requires inclusion of another peak at 780 cm^{-1} (Figure 7, top right). Fitting the signals in this region for the 60% $^{18}OH_2$ sample (Figure 7, middle right) requires the inclusion of peaks at 780 cm^{-1} and 749 cm^{-1}, which can be assigned respectively to the ν_{as}(Fe–O–Fe) modes of the ^{16}O and ^{18}O isotopomers and correspond to an ∠Fe-O-Fe of 138° on the Sanders-Loehr correlation (Figure 6), in reasonable agreement with the EXAFS-derived angle of 133°. **CmlI^{P}** thus represents the only enzymatic diiron-peroxo intermediate to have both an oxo and a peroxo bridge, a combination that presumably has implications on its biological function.

The previously reported Raman spectrum of **CmlI^{P}** identified the ν(O–O) vibration at 791 cm^{-1}, which downshifted 43 cm^{-1} when **CmlI^{P}** was formed with $^{18}O_2$. In the experiments reported here, the ν(O–O) is observed at 789 cm^{-1} and does not shift in $^{18}OH_2$ buffer. The latter result is consistent with recent mechanistic data demonstrating that water is not incorporated into the products of *N*-oxygenation by CmlI and therefore does not exchange with the bound peroxo moiety.[15]

Effect of D_2O on the Active Site

To interrogate the effect of water on the **CmlI** active site, we conducted rR experiments with **CmlI^{Ox}-D$_2$O** and **CmlI^{P}-D$_2$O**. D_2O-sensitive vibrations were observed for both **CmlI^{Ox}** and **CmlI^{P}** (Table 3). For **CmlI^{Ox}**, the ν_{s}(Fe–O–Fe) peak downshifts by 7 cm^{-1} in **CmlI^{Ox}-D$_2$O** (Figure 5, left panel, blue trace), while the ν_{as}(Fe–O–Fe) peak could not be deconvoluted from the experimental spectrum (Figure 5, left bottom). For **CmlI^{P}**, the ν_{s}(Fe–O–Fe) peak downshifts by 4 cm^{-1}, while the ν_{as}(Fe–O–Fe) peak downshifts by 2 cm^{-1}. These results indicate some interaction between the Fe–O–Fe unit and solvent water, but are different from those reported for **metHr-X** complexes,[87] the only other nonheme protein with a (μ-oxo)diferric active site that has been investigated in the same manner. Interestingly, D_2O substitution did not affect the ν_{s}(Fe–O–Fe) frequency observed for **metHr-X** complexes with X = azide, thiocyanate, cyanate, cyanide, chloride or formate. These anions occupy the only coordination site available for exogenous ligands on the diiron center of hemerythrin and preclude the possibility of water binding to this center. However respective upshifts of +4 and +26 cm^{-1} were found for X = hydroperoxide and hydroxide, anions with O–H functionalities that can hydrogen bond to the oxo bridge of the Fe–O–Fe center.[87] Clearly, D_2O interacts with the μ-oxo moiety in CmlI in a different manner from the hemerythrin complexes,[87] which we will explore in the Discussion.

The effect of D_2O on the Raman properties of the iron(III)-peroxo unit of **CmlI^{P}** (Figure 5) is also different from that on **oxyHr. OxyHr** exhibits a ν(O–O) mode at 844 cm^{-1} that upshifts by 4 cm^{-1} in the presence of D_2O and a ν(Fe–OOH) mode at 503 cm^{-1} that downshifts by 3 cm^{-1}.[88] Parallel behavior is reported for oxymyohemerythrin (oxyMHr).[91] The unusual upshift of the ν(O–O) in these two complexes reflects the hydrogen bonding

interaction between the hydroperoxo ligand and the Fe–O–Fe unit that is crucial for the reversible O_2 binding function of hemerythrin.[92] In contrast for **CmlI^P**, the ν(O–O) mode is unaffected by D_2O.

DISCUSSION

The reactions of the *N*-oxygenase CmlI and its analog AurF present the clearest examples to date of a diiron-peroxo intermediate as the major reactive species in a catalytic cycle. The peroxo intermediate involved in the 6-e$^-$-oxidation of an arylamine substrate to a nitroaryl product exhibits unique spectroscopic features that distinguish it from the commonly encountered *cis*-(μ-1,2-peroxo)diferric intermediates of other well characterized diiron cluster-containing enzymes.[8, 24, 33, 93–94] These features include its orange color and a ν(O–O) frequency that is the lowest by far found for a diferric-peroxo complex. Here, we have taken advantage of the exceptionally long lifetime of the **CmlI^P** to prepare nearly homogeneous, high concentration samples for detailed XAS and rR analysis. The results indicate that **CmlI^P** has a geometry that has not been previously described in biological or chemical systems. The basis for this assignment and the implications for the reactivity of peroxo intermediates are discussed here.

Comparison of CmlI^P to Synthetic Diferric *cis*-μ-1,2-Peroxo Intermediates

Besides its orange color and ν(O–O) frequency, perhaps the most distinguishing spectral feature of **CmlI^P** is the 2.82-Å scatterer seen in its EXAFS spectrum. Such a scatterer has not been previously reported for any diiron enzyme. To better address the assignment of this feature, available structural information from synthetic models was used to parse the possibilities. As detailed in the introduction, O_2 binds in a *cis*-μ-1,2 mode (Figure 8, A) in all crystallographically characterized synthetic diferric-peroxo species, and all except one of these have an additional single-atom bridge; examples of these complexes are listed in Table 4 and include $[Fe^{III}_2$(N-Et-HPTB)$(O_2)(Ph_3PO)_2]^{3+}$ (**9**) (N-Et-HPTB = N,N,N',N'-tetrakis(2-benzimidazolylmethyl)-2-hydroxy-1,3-diaminopropane)[30] and the acid/base pair of $[Fe^{III}_2(6Me_2\text{-BPP})_2(OH)(O_2)]^+$ (**10**) and $[Fe^{III}_2(6Me_2\text{-BPP})_2(O)(O_2)]$ (**11**) ($6Me_2$-BPP = N,N-bis(6-methyl-2-pyridylmethyl)-3-amino-propionate).[95] In these species, the Fe–O–O–Fe torsion angle is ~0°, corresponding to a nearly flat Fe1–O1–O2–Fe2 unit that fixes the distal O (Fe1•••O2 and Fe2•••O1) of the peroxo moiety to a distance of ~2.9 Å in **9** and **10** and ~3 Å in **11** (Fe•••Fe: **9** = 3.46 Å, **10** = 3.40 Å, **11** = 3.17 Å). These distances are longer than the 2.82-Å distance observed in **CmlI^P**. The metal-metal separation for **9** and **10** is ~0.1 Å longer than found for **CmlI^P**, while the oxo-bridged **11** has a metal-metal separation that is ~0.2 Å shorter than that of **CmlI^P**. Importantly, an ~2.8 Å O scatterer has not been reported in the EXAFS analyses for these synthetic peroxo species or related complexes[60–63, 83] or for the enzymatic μ-1,2-peroxo species hDOHH^P.[57] Collectively, these spectroscopic results implicate a peroxo binding geometry for **CmlI^P** that is distinct from the *cis*-μ-1,2-peroxo configuration commonly found in diiron chemistry.[8]

Comparison of CmlI^P to Known (μ-η^2: η^1-Peroxo)dimetal Complexes

In our previous study,[8] we suggested that **CmlI^P** might have a η^2: η^1-peroxo geometry because it exhibits a ν(O–O) frequency nearly identical to the 790-cm^{-1} value reported for

[(TMP-5Me-TPA)$Fe^{III}(O_2)Cu^{II}]^+$ (**12**) (TMP-5Me-TPA = 10,15,20-tris(2,4,6-trimethylphenyl)-5-(2'-bis((5''-methyl-2''-pyridylmethyl)aminomethyl)pyridine-5'-carboxyamidophenyl)-porphyrin) (Table 4).[96] This orthogonal comparison was necessary, because no synthetic (μ-η^2:η^1-peroxo)diferric complex had yet been reported. In the crystal structure of the Fe/Cu complex **12** reported by Naruta,[96] O_2 is bound η^2 to Fe and η^1 to Cu (Figure 8, B), Its structure shows a flat Fe–O–O–Cu plane, with Fe–O_{peroxo} distances of 1.89 and 2.03 Å, Cu–O_{peroxo} distances of 1.92 and 2.66 Å, and an Fe•••Cu separation of 3.92 Å, which is much longer than observed for **CmlI^P**. Moreover, there would be no way to accommodate a 2.82 Å scatterer with an η^2:η^1 configuration. Although there is a Cu-O_{distal} distance in **12** of 2.66 Å, the corresponding Fe-O_{distal} distance at 2.03 Å, so this (μ-η^2:η^1-peroxo)dimetal core would not be a suitable model for the core deduced for **CmlI^P** by EXAFS analysis.

Another crystallized complex with a μ-η^2:η^1-peroxo ligand is [(oxapyme)Co^{III}_2(μ-η^2:η^1-O_2)]$^{2+}$ (**13**) (oxapyme = 2-(bis-pyridin-2-ylmethyl-amino)-*N*-[2-(5-{2-[2-(methyl-pyridin-2-ylmethyl-amino)-acetylamino]-phenyl}-[1,3,4]oxadiazol-2-yl)-phenyl]-acetamide) (Figure 8, B).[97] This complex has a Co•••Co separation of 3.34 Å, with Co1– η^2 -O_{peroxo} bond lengths of 1.85 and 1.93 Å and Co2–η^1-O_{peroxo} distances of 1.92 and 2.76 Å. Although the metal-metal separation matches that of **CmlI^P**, only one of the two Co centers has a Co-O_{distal} distance that approaches the 2.8-Å distance found in **CmlI^P**, as with the Fe/Cu complex discussed above. Furthermore, neither of the two (μ-η^2:η^1-peroxo)dimetal complexes discussed has the additional oxo bridge found in **CmlI^P** by rRaman and EXAFS analysis.

Complex **13** provides an additional point of comparison because a related complex **14**, [(oxapyme)Co^{III}_2(μ-1,2-O_2)(NO_2)]$^{1+}$, has been described, and both complexes have been analyzed by FT-Raman. Complex **13** has a ν(O–O) = 839 cm^{-1}, with no ν(Co–O–Co) vibration reported, and **14** has a ν(O–O) of 866 cm^{-1}. A change in the O–O stretching frequency of -27 cm^{-1} is observed on going from a μ-1,2-peroxo binding mode in **14** to a μ-η^2:η^1 configuration in **13**,. In contrast, the ν(O–O) for **CmlI^P** is at least 60 cm^{-1} lower in energy than found for any (*cis*-μ-1,2-peroxo)diferric intermediates.[8] This structural and vibrational analysis argues against the η^2:η^1-O_2 assignment for **CmlI^P**.

The μ-1,1-Peroxo Model for CmlI^P

An alternative to the *cis*-μ-1,2-peroxo and μ-η^2:η^1 peroxo configurations is the μ-1,1-peroxo mode illustrated in Figure 8C. The analysis of the XAS data shows that **CmlI^{Ox}** and **CmlI^P** have very similar diiron(III) core structures, including short Fe–μ-O distances of 1.83 Å indicative of an oxo bridge and identical Fe•••Fe distances (Figure 9 and Table 2). A μ-1,1-peroxo ligand would provide an explanation for the unique 2.82 Å scatterer found in **CmlI^P**. To rationalize the low σ^2 associated with this scatterer, the distal oxygen of the peroxo unit must be at approximately this distance from each iron. The only other scatterer with a similar distance and comparably small σ^2 is the carbon atom of the bidentate carboxylates at ~2.6 Å seen in the **CmlI^R** sample. It could be argued that bidentate carboxylate ligand(s) of **CmlI^R** could become monodentate upon formation of **CmlI^P**, which would increase the Fe–C distance to 2.82 Å as observed in **CmlI^P**. However, such a

monodentate ligand would not be expected to have the rigidity to give rise to the observed 2.82-Å scatterer; indeed scattering from such a ligand has not been reported previously in EXAFS studies of diiron enzymes. The model for **CmlI^{P}** as a μ-1,1-peroxo species based on the XAS and rR data presented here is compared with those for **CmlI^{Ox}** and **CmlI^{R}** in Figure 9.

Support for the Assignment of the 2.8-Å Scatterer from the Structure of Product-Bound AurF

Further support for the assignment of the 2.82-Å scatterer as the terminal oxygen of a μ-1,1-peroxo unit comes from the crystal structure of AurF with product bound (PDB code 3CHT).[7] The product of the AurF-catalyzed reaction is *para*-nitrobenzoic acid (pNBA), which is bound in the active site substrate channel with one of the oxygen atoms of the nitro group oriented between the two Fe centers (Figure 10). If the peroxo intermediate of AurF also adopts the proposed μ-1,1-peroxo binding configuration, it would place the distal peroxo oxygen at approximately the position of one of the O atoms of the nitro group that is formed during the reaction. This juxtaposition should facilitate oxygen atom transfer to the precursor aryl-nitroso intermediate during the reaction. The product-bound AurF crystal structure also suggests a means by which the terminal oxygen of the μ-1,1-peroxo can be rigidly positioned, as reflected in the small $\boldsymbol{\sigma}^2$ value observed for the 2.82-Å scatterer (Table 2). Three of the monodentate carboxylate ligands of the AurF diiron center (Figure 10, labeled 1 – 3) have their distal oxygen atoms pointing into the substrate pocket within 2.8 to 3.1 Å of the oxygen atom of pNBA. These residues are all conserved in the active site pocket of CmlI. Steric interactions may lock the peroxo moiety in the optimal position for reaction. The constrained orientation of the peroxo ligand may also distort the iron coordination geometry sufficiently to account for the unusually large XAS pre-edge feature of **CmlI^{P}**.

Comparison of CmlI^{P} to Known μ-1,1-Peroxo Complexes

Examples of dinuclear complexes with a μ-1,1-(hydro)peroxo ligand are quite scarce. $[Cu^{II}_2(L^{et})(OOH)](OTf)(BPh_4)$ (**15**) (L^{et} = 3,5-bis(1-ethyl-4,7-di-*iso*propyl-1,4,7-triazacyclononane)pyrazole) is a crystallographically characterized example of a (μ-1,1-hydroperoxo)dicopper complex reported by Meyer and co-workers.[98] This complex has a nearly planar Cu–O_2–Cu core with a metal-metal distance of 3.53 Å, which is ~0.2 Å longer than that in **CmlI^{P}** due to the pyrazolate bridge in **15**. Interestingly, both Cu atoms are approximately 2.95 Å from the O_{distal}-atom, which is longer than the 2.82 Å distance found for **CmlI^{P}**; however this distance can be shortened by tilting the O–O bond out of the Cu–$O_{proximal}$–Cu plane, as we propose in the case of **CmlI^{P}**. The rR spectrum of **15** shows a higher ν(O–O) frequency than what is observed for **CmlI^{P}** (860 cm^{-1} vs 789 cm^{-1}),[98] but the authors mention that there is significant mechanical coupling between the ν(O–O) and ν(Cu–O), which makes direct comparison to the ν(O–O) of **CmlI^{P}** challenging.

Among the recently reported crystallographic results for T4MO is the crystal structure of the unreactive O_2 adduct of the Q228A variant of reduced T4MOH in complex with its effector protein D.[35] This structure shows a diiron center with an Fe•••Fe distance of 3.3 Å and μ-1,1-dioxygen bridge, the 1.5-Å O•••O distance of which is indicative of a peroxide ligand. The observed Fe–O_{distal} distances of 3.2 – 3.7 Å are quite a bit longer than those found for

CmlI^{P}, suggesting that the (μ-1,1-peroxo)diiron(III) unit in this T4MO adduct is much closer to a plane than that found in **CmlI^{P}**. As the distal O-atom of the μ-1,1-peroxo ligand in the Q228A T4MOH adduct occupies the same space as C-3 of the toluene substrate, it seems unlikely to be a catalytically viable intermediate in the T4MOHD cycle.

Structural Effects of Protonation or Hydrogen Bonding in the CmlI^{P} Active Site

The rR analysis of **CmlI^{P}** and **CmlI^{Ox}** demonstrate that the ν(Fe–O–Fe) vibrations are affected by substitution with D_2O. The only other diiron protein for which D_2O isotope shifts have been reported is **oxyHr**. Sanders-Loehr and co-workers showed that the isotope shift from D_2O in **oxyHr** was the result of hydrogen bonding interactions between the end-on hydroperoxo ligand and the μ-oxo bridge.[87] Along similar lines, the D_2O isotope shift in CmlI presumably results from hydrogen bonding as well. However for **CmlI^{P}**, the hydrogen bonding interaction cannot arise from a hydroperoxo ligand, as the ν(O–O) is not affected by D_2O substitution, unlike in the case of **oxyHr**, where the ν(O–O) of the OOH ligand is in fact upshifted upon deuterium substitution.[88] Protonation of the μ-oxo ligand can also be ruled out based on precedent from synthetic complexes. Direct protonation of an oxo bridge substantially lengthens the Fe-μ-O bond and decreases the ν_s(Fe–O–Fe) frequency. This effect is demonstrated in the case of the (μ-oxo)(μ-1,2-peroxo)diferric complex **1**. When **1** is protonated to its μ-hydroxo conjugate acid, the Fe-μ-O bond lengthens by 0.1 Å from 1.81 to 1.91 Å, and the ν_s(Fe–O–Fe) vibration decreases by ~100 cm^{-1}, from 523 cm^{-1} in **1** to 424 cm^{-1}.[60] Neither of these changes is observed in the comparison of **CmlI^{P}** with **CmlI^{Ox}**, so the oxo bridge does not become protonated.

One possible source of hydrogen bonding interactions with the Fe–O–Fe unit is a protonated protein ligand. E236 in the crystal structure of CmlI is able to move to the proposed position of the μ-oxo ligand, so if protonated, E236 could feasibly interact with the Fe–O–Fe unit in both **CmlI^{Ox}** and **CmlI^{P}**.[39] However, at pH = 9 for the CmlI samples, it is not likely for the carboxylate residues to be protonated. A likely alternative is that water hydrogen bonds to the oxo bridge, accounting for its observed rR shift and the lower ν_s(Fe–O–Fe) relative to values for metHr-X and related synthetic complexes (Table 3). This hydrogen bond would also serve to distribute the formal -2 charge on the **CmlI^{P}** cluster, which is the largest known among biological diiron cluster complexes.

Disparity Between XAS and XRD of the CmlI Peroxo Intermediate

The structural model for **CmlI^{P}** that has been developed here differs substantially from that of the peroxo intermediate seen in the XRD structure of **CmlIΔ33**, revealing a (*cis*-μ-1,2-peroxo)diiron center without an oxo bridge.[39] Similarly, the structural details of the **CmlI^{R}** state determined here differ in several aspects from what is found in the crystal structure of **CmlIΔ33^{R}**. Differences may arise from the inherent differences in crystallized versus solution state intermediates and/or from the different pH values at which the samples were prepared, pH 6.3 for the crystallization and pH 9 for our spectroscopic studies. It is likely that the structures derived from XAS and rR data more accurately reflect the active enzyme, because these samples are made directly from solution. In contrast, the peroxo intermediate found in the crystal is thought to be generated by diffusion into the crystal of H_2O_2 formed as PEG in the mother liquor breaks down.[39] Similarly, the reduced state in the crystal is

generated by diffusion of a reductant into the pre-formed crystal. In each case, the active site structure in the crystal forces an amino acid side chain into the substrate binding channel, so the enzyme is unlikely to be active. The same inactive conformation is seen in the crystal structure for the dimanganese form of AurF,[99] but not the native diiron form, which exhibits an open substrate binding channel.[7] AurF also does not spontaneously form a *cis*-μ-1,2-peroxo intermediate in the crystal of the resting diferric enzyme.

Comparison with Proposed Structure of AurF^{P}

Recently, a model for AurF^{P} has been advanced based on NRVS (nuclear resonance vibrational spectroscopy) and associated computational studies.[100] This model of AurF^{P} contains a protonated *cis*-μ-1,2-peroxo bridge. Like the (μ-oxo)(μ-1,1-peroxo)diferric species proposed for the homologous **CmlI^{P}**, the protonated *cis*-μ-1,2-peroxo bridging structure proposed for AurF^{P} is without synthetic precedent, so the interpretation of the NRVS data has been facilitated by computational simulation. The rR spectra presented here for **CmlI^{P}** show no evidence for protonation of the peroxo unit. The protonation state of the bound peroxo unit can be best ascertained by the observation of a ^{2}H-isotope shift in the ν(Fe–OOH) mode, as seen for **oxyHr**[87] and two synthetic Fe–OOH complexes,[101–102] but this mode has not been identified in the rR spectrum of **CmlI^{P}**. In the computational study of AurF^{P}, the authors tested a (μ-1,1-peroxo)diferric model and found that it could not reproduce the experimental NRVS spectra. However, the authors did not test a (μ-oxo)(μ-1,1-peroxo)diferric model similar to the model proposed here for **CmlI^{P}**, evidence for the oxo bridge having just been obtained by XAS and rR in the present study. In fact, in all of the models computed in the AurF^{P} study, the carboxylate equivalent to E236 of CmlI acts as a bidentate bridge, as found in the crystal structure of dimanganese(II) AurF.[7] This differs from the reported X-ray crystal structures for diiron(III) AurF[7] and, as related above, is unlikely to be active because it forces the substrate binding channel to close. It is interesting to note that the AurF^{P} study finds that the protonated *cis*-μ-1,2-peroxo intermediate is unlikely to undergo O–O bond cleavage, as the frontier molecular orbitals are unfavorably oriented for a reaction with the pNBA substrate. Indeed, reorganization to a (μ-1,1-peroxo)diferric species is predicted to dramatically lower the energy barrier of the native reaction, relative to the protonated *cis*-μ-1,2-peroxo model. Thus, a peroxo-diferric species with a structure similar to what we propose for **CmlI^{P}** is also likely to be implicated in the *N*-oxygenation reaction of the AurF system.

Possible Mechanism for O–O Bond Cleavage in CmlI^{P}

In light of the updated structure of **CmlI^{P}** as well as mechanistic studies,[15] we can better assess how **CmlI^{P}** carries out reactions with the native substrate. During the course of the native reaction, **CmlI^{P}** is capable of oxidizing the more electron-rich aryl-amine substrate (Figure 1, left), as well as a less electron-rich aryl-nitroso substrate later in the reaction pathway.[15] These mechanistic traits require **CmlI^{P}** to be ambiphilic, being able to switch from being an electrophilic oxidant in the oxidation of the aryl-amine to acting as a nucleophilic oxidant in the oxidation of the aryl-nitroso substrate. The available kinetic data suggest a direct reaction between substrate and **CmlI^{P}** without an intervening a high-valent intermediate typically encountered in diiron oxygenases that activate C–H bonds. This

ambiphilic reactivity is unprecedented for a peroxo intermediate, but does not extend to the activation of C–H bonds.[8, 15] There are two major differences between the proposed **CmlI^{P}** structure and the canonical *cis*-μ-1,2 peroxo species. In the latter, both oxygen atoms are tethered to an iron atom, thereby decreasing its accessibility to substrate as well as limiting its reactivity. Subsequent protonation is a common strategy for enhancing its reactivity, by conversion of the *cis*-μ-1,2 peroxo species to a high-valent oxidant. On the other hand, the postulated terminally bound and unprotonated peroxo unit of **CmlI^{P}** is more versatile and can react directly with both its amino- and nitroso-substituted substrates

As indicated in Figure 11, the placement of an unprotonated terminal oxygen of a peroxo intermediate immediately next to the position for oxygen transfer to the substrate would allow either nucleophilic or electrophilic reactions. In the first step of the native reaction (Figure 11, A), the substrate amine group would likely be protonated under the reaction conditions and provide the proton required to break the O–O bond in the hydroxylation of the amine function, thereby linking O–O bond cleavage with substrate hydroxylation. In the later step of the biosynthetic pathway, the nitroso substrate would be susceptible to direct nucleophilic attack by the peroxo ligand (Figure 11, B), resulting in heterolytic cleavage of the peroxo bond to generate the chloramphenicol product and a diferric cluster.

CONCLUSION

Enzymatic peroxo-diferric intermediates have been known for several decades, but every structurally characterized example, until very recently, has contained a μ-1,2-peroxo binding mode.[103] **CmlI^{P}** is proposed here to have a μ-oxo bridge as well as a μ-1,1-peroxo ligand that interacts with protein-derived ligands in the CmlI active site. It is the only example of a μ-1,1-peroxo species in diiron chemistry. Despite having the same 4α-helix fold and a similar active site as C–H activating enzymes like sMMOH, CmlI is unable to facilitate C–H bond oxidation. It seems likely that the novel peroxo structure increases its reactivity over the canonical peroxo intermediate. This boost in oxidizing potency then allows it to carry out both electrophilic and nucleophilic *N*-oxygenations without creating a species that can also carry out adventitious C–H bond activation reactions.

Supplementary Material

Refer to Web version on PubMed Central for supplementary material.

Acknowledgments

The authors acknowledge financial support of this work from grants NIH GM118030 (to J.D.L.), NIH GM38767 (to L.Q.) and graduate traineeship NIH GM08700 (to A.J.K.). XAS data were collected on Beamlines 7-3 and 9-3 at the Stanford Synchrotron Radiation Lightsource, SLAC National Accelerator Laboratory. SLAC is supported by the U.S. Department of Energy (DOE), Office of Science, Office of Basic Energy Sciences under Contract No. DE-AC02-76SF00515. Use of Beamlines 7-3 and 9-3 is supported by the DOE Office of Biological and Environmental Research and the National Institutes of Health, National Institute of General Medical Sciences (including P41GM103393). We thank Brent Rivard for assistance with protein growth and helpful discussions.

ABBREVIATIONS USED

AurF	arylamine oxygenase of the aureothin biosynthesis pathway

cADO	cyanobacterial aldehyde deformylating oxygenase
CmlA	*β*-hydroxylase of the chloramphenicol biosynthetic pathway
CmlI	arylamine oxygenase of the chloramphenicol biosynthetic pathway
CmlIΔ33	33-amino-acid-truncated form of CmlI
CmlI^{Ox}	as-isolated diferric CmlI
CmlI^{Ox}-D$_2$O	as-isolated diferric CmlI in D_2O buffer
CmlI^{P}	peroxo-diferric intermediate of CmlI
CmlI^{P}-D$_2$O	peroxo-diferric intermediate of CmlI prepared in D_2O buffer
CmlI^{R}	chemically reduced CmlI with a diferrous cluster
Δ^{9}D	stearoyl-CoA Δ^9-desaturase
EXAFS	extended X-ray absorption fine structure
FT	Fourier transform
hDOHH	human deoxyhypusine hydroxylase
LN$_2$	liquid nitrogen
sMMOH	the hydroxylase subunit of the soluble form of methane monooxygenase
oxyHr	the oxygenated form of hemerythrin
pNBA	*p*-nitrobenzoic acid
RNR R2	the diiron-cluster-containing subunit of ribonucleotide reductase
T4MO	toluene-4-monooxygenase
ToMO	toluene/o-xylene monooxygenase
rR	resonance Raman spectroscopy
XAS	X-ray absorption spectroscopy
XANES	X-ray absorption near-edge structure

References

1. Wallar BJ, Lipscomb JD. Chem Rev. 1996; 96:2625–2657. [PubMed: 11848839]

2. Pikus JD, Studts JM, Achim C, Kauffmann KE, Münck E, Steffan RJ, McClay K, Fox BG. Biochemistry. 1996; 35:9106–9119. [PubMed: 8703915]
3. Bochevarov AD, Li J, Song WJ, Friesner RA, Lippard SJ. J Am Chem Soc. 2011; 133:7384–7397. [PubMed: 21517016]
4. Fox BG, Lyle KS, Rogge CE. Acc Chem Res. 2004; 37:421–429. [PubMed: 15260504]
5. Krebs C, Bollinger JM Jr, Booker SJ. Curr Opin Chem Biol. 2011; 15:291–303. [PubMed: 21440485]
6. Das D, Eser BE, Han J, Sciore A, Marsh ENG. Angew Chem Int Ed. 2011; 50:7148–7152.
7. Choi YS, Zhang H, Brunzelle JS, Nair SK, Zhao H. Proc Natl Acad Sci USA. 2008; 105:6858–6863. [PubMed: 18458342]
8. Makris TM, Vu VV, Meier KK, Komor AJ, Rivard BS, Münck E, Que L Jr, Lipscomb JD. J Am Chem Soc. 2015; 137:1608–1617. [PubMed: 25564306]
9. Lu HG, Chanco E, Zhao HM. Tetrahedron. 2012; 68:7651–7654.
10. Makris TM, Chakrabarti M, Münck E, Lipscomb JD. Proc Natl Acad Sci USA. 2010; 107:15391–15396. [PubMed: 20713732]
11. Fischbach MA, Walsh CT. Chem Rev. 2006; 106:3468–3496. [PubMed: 16895337]
12. Walsh CT, Chen H, Keating TA, Hubbard BK, Losey HC, Luo L, Marshall CG, Miller DA, Patel HM. Curr Opin Chem Biol. 2001; 5:525–534. [PubMed: 11578925]
13. Pacholec M, Sello JK, Walsh CT, Thomas MG. Org Biomol Chem. 2007; 5:1692–1694. [PubMed: 17520135]
14. Piraee M, White RL, Vining LC. Microbiology. 2004; 150:85–94. [PubMed: 14702400]
15. Komor AJ, Rivard BS, Fan R, Guo Y, Que L Jr, Lipscomb JD. J Am Chem Soc. 2016; 138:7411–7421. [PubMed: 27203126]
16. Sturgeon BE, Burdi D, Chen S, Huynh BH, Edmondson DE, Stubbe J, Hoffman BM. J Am Chem Soc. 1996; 118:7551–7557.
17. Doan PE, Shanmugam M, Stubbe J, Hoffman BM. J Am Chem Soc. 2015; 137:15558–15566. [PubMed: 26636616]
18. Dassama LMK, Silakov A, Krest CM, Calixto JC, Krebs C, Bollinger JM Jr, Green MT. J Am Chem Soc. 2013; 135:16758–16761. [PubMed: 24094084]
19. Lee SK, Lipscomb JD. Biochemistry. 1999; 38:4423–4432. [PubMed: 10194363]
20. Liu KE, Wang D, Huynh BH, Edmondson DE, Salifoglou A, Lippard SJ. J Am Chem Soc. 1994; 116:7465–7466.
21. Han WG, Noodleman L. Inorg Chem. 2008; 47:2975–86. [PubMed: 18366153]
22. Skulan AJ, Brunold TC, Baldwin J, Saleh L, Bollinger JM Jr, Solomon EI. J Am Chem Soc. 2004; 126:8842–8855. [PubMed: 15250738]
23. Bollinger JM Jr, Krebs C, Vicol A, Chen S, Ley BA, Edmondson DE, Huynh BH. J Am Chem Soc. 1998; 120:1094–1095.
24. Moenne-Loccoz P, Baldwin J, Ley BA, Loehr TM, Bollinger JM Jr. Biochemistry. 1998; 37:14659–14663. [PubMed: 9778340]
25. Broadwater JA, Achim C, Münck E, Fox BG. Biochemistry. 1999; 38:12197–12204. [PubMed: 10493786]
26. Beauvais LG, Lippard SJ. J Am Chem Soc. 2005; 127:7370–7378. [PubMed: 15898785]
27. Tinberg CE, Lippard SJ. Biochemistry. 2010; 49:7902–7912. [PubMed: 20681546]
28. Ookubo T, Sugimoto H, Nagayama T, Masuda H, Sato T, Tanaka K, Maeda Y, Okawa H, Hayashi Y, Uehara A, Suzuki M. J Am Chem Soc. 1996; 118:701–702.
29. Menage S, Brennan BA, Juarez-Garcia C, Münck E, Que L Jr. J Am Chem Soc. 1990; 112:6423–6425.
30. Dong Y, Yan S, Young VG Jr, Que L Jr. Angew Chem Int Ed. 1996; 35:618–620.
31. Kim K, Lippard SJ. J Am Chem Soc. 1996; 118:4914–4915.
32. Zhang X, Furutachi H, Fujinami S, Nagatomo S, Maeda Y, Watanabe Y, Kitagawa T, Suzuki M. J Am Chem Soc. 2005; 127:826–827. [PubMed: 15656607]

33. Vu VV, Emerson JP, Martinho M, Kim YS, Münck E, Park MH, Que L Jr. Proc Natl Acad Sci USA. 2009; 106:14814–14819. [PubMed: 19706422]
34. Pandelia ME, Li N, Noergaard H, Warui DM, Rajakovich LJ, Chang W-c, Booker SJ, Krebs C, Bollinger JM Jr. J Am Chem Soc. 2013; 135:15801–15812. [PubMed: 23987523]
35. Acheson JF, Bailey LJ, Brunold TC, Fox BG. Nature. 2017; 544:191–195. [PubMed: 28346937]
36. Murray LJ, Naik SG, Ortillo DO, Garcia-Serres R, Lee JK, Huynh BH, Lippard SJ. J Am Chem Soc. 2007; 129:14500–14510. [PubMed: 17967027]
37. Song WJ, Behan RK, Naik SG, Huynh BH, Lippard SJ. J Am Chem Soc. 2009; 131:6074–6075. [PubMed: 19354250]
38. Han Z, Sakai N, Boettger LH, Klinke S, Hauber J, Trautwein AX, Hilgenfeld R. Structure. 2015; 23:882–892. [PubMed: 25865244]
39. Knoot CJ, Kovaleva EG, Lipscomb JD. J Biol Inorg Chem. 2016; 21:589–603. [PubMed: 27229511]
40. Bailey LJ, Fox BG. Biochemistry. 2009; 48:8932–8939. [PubMed: 19705873]
41. Sousa CM, Carpentier P, Matias PM, Testa F, Pinho F, Sarti P, Giuffrè A, Bandeiras TM, Romão CV. Acta Crystallogr D Biol Crystallogr. 2015; 71:2236–2247. [PubMed: 26527141]
42. Gudmundsson M, Kim S, Wu M, Ishida T, Momeni MH, Vaaje-Kolstad G, Lundberg D, Royant A, Ståhlberg J, Eijsink VGH, Beckham GT, Sandgren M. J Biol Chem. 2014; 289:18782–18792. [PubMed: 24828494]
43. Sigfridsson KGV, Chernev P, Leidel N, Popovic-Bijelic A, Gräslund A, Haumann M. J Biol Chem. 2013; 288:9648–9661. [PubMed: 23400774]
44. Andersson KK, Froland WA, Lee SK, Lipscomb JD. New J Chem. 1991; 15:411–415.
45. Korboukh VK, Li N, Barr EW, Bollinger JM Jr, Krebs C. J Am Chem Soc. 2009; 131:13608–13609. [PubMed: 19731912]
46. Chufan EE, Puiu SC, Karlin KD. Acc Chem Res. 2007; 40:563–572. [PubMed: 17550225]
47. Naruta Y, Sasaki T, Tani F, Tachi Y, Kawato N, Nakamura N. J Inorg Biochem. 2001; 83:239–246. [PubMed: 11293543]
48. Li F, Van HKM, Meier KK, Münck E, Que L Jr. J Am Chem Soc. 2013; 135:10198–10201. [PubMed: 23802702]
49. Lee YM, Bang S, Kim YM, Cho J, Hong S, Nomura T, Ogura T, Troeppner O, Ivanovic-Burmazovic I, Sarangi R, Fukuzumi S, Nam W. Chem Sci. 2013; 4:3917–3923. [PubMed: 25426288]
50. George GN. A suite of computer programs for analysis of X-ray absorption spectra. 1990
51. Ankudinov AL, Ravel B, Rehr JJ, Conradson SD. Phys Rev B. 1998; 58:7565–7576.
52. Westre TE, Kennepohl P, DeWitt JG, Hedman B, Hodgson KO, Solomon EI. J Am Chem Soc. 1997; 119:6297–6314.
53. Wojdyr M. J Appl Crystallogr. 2010; 43:1126–1128.
54. Menges, F. Spekwin32 - optical spectroscopy software, 1.72.0. 2015.
55. Griese JJ, Kositzki R, Schrapers P, Branca RMM, Nordström A, Lehtiö J, Haumann M, Högbom M. J Biol Chem. 2015; 290:25254–25272. [PubMed: 26324712]
56. Hwang J, Krebs C, Huynh BH, Edmondson DE, Theil EC, Penner-Hahn JE. Science. 2000; 287:122–125. [PubMed: 10615044]
57. Jasniewski AJ, Engstrom LM, Vu VV, Park MH, Que L. J Biol Inorg Chem. 2016; 21:605–618. [PubMed: 27380180]
58. Jasniewski AJ, Knoot CJ, Lipscomb JD, Que L Jr. Biochemistry. 2016; 55:5818–5831. [PubMed: 27668828]
59. Vu VV, Makris TM, Lipscomb JD, Que L Jr. J Am Chem Soc. 2011; 133:6938–6941. [PubMed: 21506543]
60. Cranswick MA, Meier KK, Shan X, Stubna A, Kaizer J, Mehn MP, Münck E, Que L Jr. Inorg Chem. 2012; 51:10417–10426. [PubMed: 22971084]
61. Pap JS, Cranswick MA, Balogh-Hergovich E, Barath G, Giorgi M, Rohde GT, Kaizer J, Speier G, Que L Jr. Eur J Inorg Chem. 2013; 2013:3858–3866. [PubMed: 24587695]

62. Fiedler AT, Shan X, Mehn MP, Kaizer J, Torelli S, Frisch JR, Kodera M, Que L Jr. J Phys Chem A. 2008; 112:13037–13044. [PubMed: 18811130]
63. Frisch JR, Vu VV, Martinho M, Münck E, Que L Jr. Inorg Chem. 2009; 48:8325–8336. [PubMed: 19610611]
64. de Groot F. Chem Rev. 2001; 101:1779–1808. [PubMed: 11709999]
65. Sarangi R. Coord Chem Rev. 2013; 257:459–472. [PubMed: 23525635]
66. Randall CR, Shu L, Chiou YM, Hagen KS, Ito M, Kitajima N, Lachicotte RJ, Zang Y, Que L Jr. Inorg Chem. 1995; 34:1036–1039.
67. Roe AL, Schneider DJ, Mayer RJ, Pyrz JW, Widom J, Que L Jr. J Am Chem Soc. 1984; 106:1676–1681.
68. Rudd DJ, Sazinsky MH, Lippard SJ, Hedman B, Hodgson KO. Inorg Chem. 2005; 44:4546–4554. [PubMed: 15962961]
69. Shu L, Broadwater JA, Achim C, Fox BG, Münck E, Que L Jr. J Biol Inorg Chem. 1998; 3:392–400.
70. Makris TM, Knoot CJ, Wilmot CM, Lipscomb JD. Biochemistry. 2013; 52:6662–6671. [PubMed: 23980641]
71. Whittington DA, Lippard SJ. J Am Chem Soc. 2001; 123:827–838. [PubMed: 11456616]
72. Elango N, Radhakrishnan R, Froland WA, Wallar BJ, Earhart CA, Lipscomb JD, Ohlendorf DH. Protein Sci. 1997; 6:556–568. [PubMed: 9070438]
73. Logan DT, Su XD, Aberg A, Regnstrom K, Hajdu J, Eklund H, Nordlund P. Structure. 1996; 4:1053–1064. [PubMed: 8805591]
74. Eriksson M, Jordan A, Eklund H. Biochemistry. 1998; 37:13359–13369. [PubMed: 9748343]
75. Lindqvist Y, Huang WJ, Schneider G, Shanklin J. EMBO. 1996; 15:4081–4092.
76. Holmes MA, Le Trong I, Turley S, Sieker LC, Stenkamp RE. J Mol Biol. 1991; 218:583–593. [PubMed: 2016748]
77. Holmes MA, Stenkamp RE. J Mol Biol. 1991; 220:723–737. [PubMed: 1870128]
78. Korendovych IV, Kryatov SV, Reiff WM, Rybak-Akimova EV. Inorg Chem. 2005; 44:8656–8658. [PubMed: 16296818]
79. Kryatov SV, Taktak S, Korendovych IV, Rybak-Akimova EV, Kaizer J, Torelli S, Shan X, Mandal S, MacMurdo VL, Mairata i Payeras A, Que L Jr. Inorg Chem. 2005; 44:85–99. [PubMed: 15627364]
80. Chaudhury P, Wieghardt K, Nuber B, Weiss J. Angew Chem Int Ed. 1985; 24:778–779.
81. True AE, Scarrow RC, Randall CR, Holz RC, Que L Jr. J Am Chem Soc. 1993; 115:4246–4255.
82. Sanders-Loehr J, Wheeler WD, Shiemke AK, Averill BA, Loehr TM. J Am Chem Soc. 1989; 111:8084–8093.
83. Dong Y, Zang Y, Kauffmann K, Shu L, Wilkinson EC, Münck E, Que L Jr. J Am Chem Soc. 1997; 119:12683–12684.
84. Wilkinson EC, Dong YH, Zang Y, Fujii H, Fraczkiewicz R, Fraczkiewicz G, Czernuszewicz RS, Que L Jr. J Am Chem Soc. 1998; 120:955–962.
85. Zheng H, Zang Y, Dong Y, Young VG Jr, Que L Jr. J Am Chem Soc. 1999; 121:2226–2235.
86. Xue G, Wang D, De Hont R, Fiedler AT, Shan X, Münck E, Que L Jr. Proc Natl Acad Sci USA. 2007; 104:20713–20718. [PubMed: 18093922]
87. Shiemke AK, Loehr TM, Sanders-Loehr J. J Am Chem Soc. 1986; 108:2437–2443. [PubMed: 22175597]
88. Shiemke AK, Loehr TM, Sanders-Loehr J. J Am Chem Soc. 1984; 106:4951–4956.
89. Norman RE, Yan S, Que L, Backes G, Ling J, Sanders-Loehr J, Zhang JH, O'Connor CJ. J Am Chem Soc. 1990; 112:1554–1562.
90. Armstrong WH, Lippard SJ. J Am Chem Soc. 1984; 106:4632–4633.
91. Xiong J, Phillips RS, Kurtz DM Jr, Jin S, Ai J, Sanders-Loehr J. Biochemistry. 2000; 39:8526–8536. [PubMed: 10913259]
92. Brunold TC, Solomon EI. J Am Chem Soc. 1999; 121:8288–8295.

93. Broadwater JA, Ai J, Loehr TM, Sanders-Loehr J, Fox BG. Biochemistry. 1998; 37:14664–14671. [PubMed: 9778341]

94. Moenne-Loccoz P, Krebs C, Herlihy K, Edmondson DE, Theil EC, Huynh BH, Loehr T. Biochemistry. 1999; 38:5290–5295. [PubMed: 10220314]

95. Zhang X, Furutachi H, Fujinami S, Nagatomo S, Maeda Y, Watanabe Y, Kitagawa T, Suzuki M. J Am Chem Soc. 2005; 127:826–827. [PubMed: 15656607]

96. Chishiro T, Shimazaki Y, Tani F, Tachi Y, Naruta Y, Karasawa S, Hayami S, Maeda Y. Angew Chem Int Ed. 2003; 42:2788–2791.

97. Gavrilova AL, Qin CJ, Sommer RD, Rheingold AL, Bosnich B. J Am Chem Soc. 2002; 124:1714–1722. [PubMed: 11853448]

98. Kindermann N, Dechert S, Demeshko S, Meyer F. J Am Chem Soc. 2015; 137:8002–8005. [PubMed: 26061290]

99. Zocher G, Winkler R, Hertweck C, Schulz GE. J Mol Biol. 2007; 373:65–74. [PubMed: 17765264]

100. Park K, Li N, Kwak Y, Srnec M, Bell CB, Liu LV, Wong SD, Yoda Y, Kitao S, Seto M, Hu M, Zhao J, Krebs C, Bollinger JM Jr, Solomon EI. J Am Chem Soc. 2017; 139:7062–7070. [PubMed: 28457126]

101. Ho RYN, Roelfes G, Feringa BL, Que L Jr. J Am Chem Soc. 1999; 121:264–265.

102. Wada A, Ogo S, Nagatomo S, Kitagawa T, Watanabe Y, Jitsukawa K, Masuda H. Inorg Chem. 2002; 41:616–618. [PubMed: 11849054]

103. Trehoux A, Mahy J-P, Avenier F. Coord Chem Rev. 2016; 322:142–158.

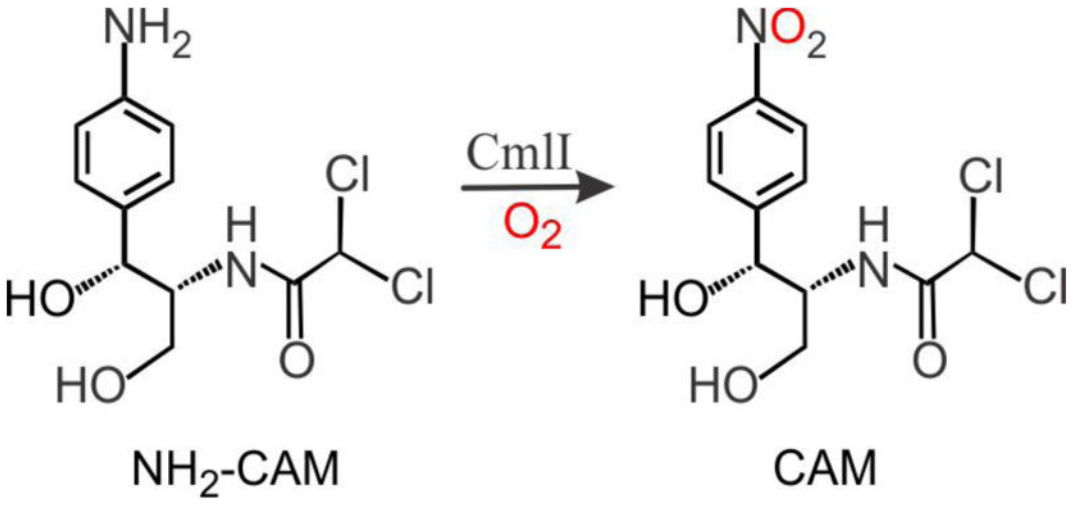

Figure 1.

Six-electron oxidation of the aryl-amine precursor to the nitroaryl-containing final product chloramphenicol, catalyzed by the nonheme diiron cluster enzyme CmlI.

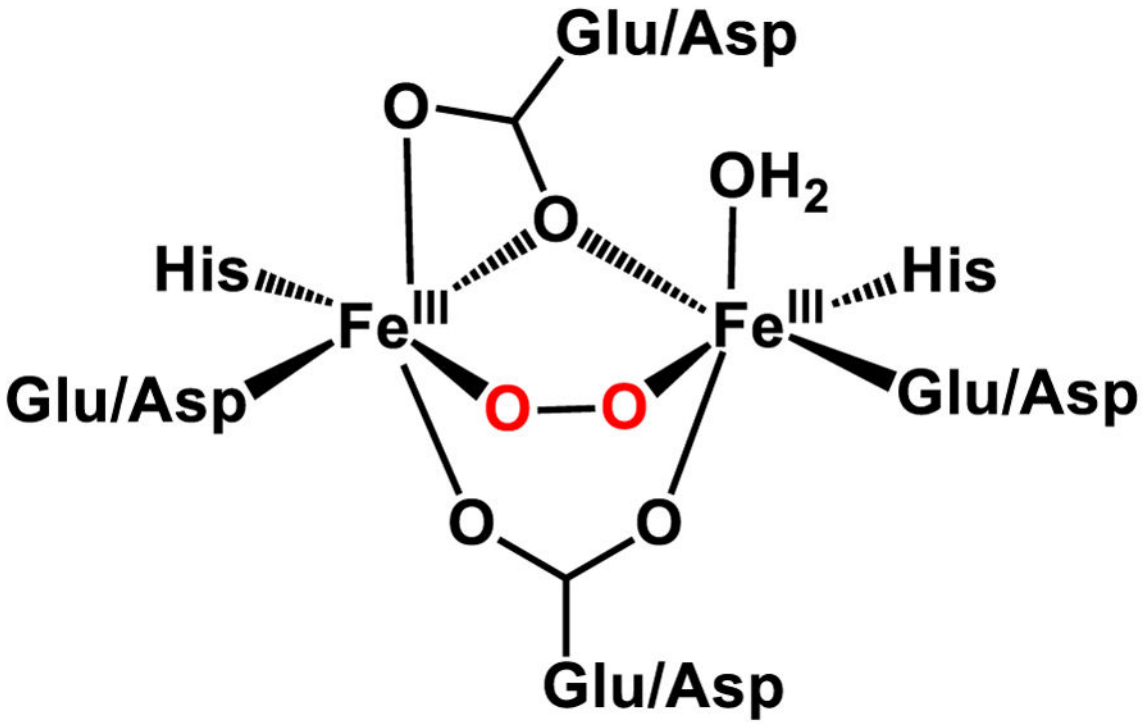

Figure 2.
General *cis*-(μ-1,2-peroxo)diferric intermediate structure in diiron enzymes.

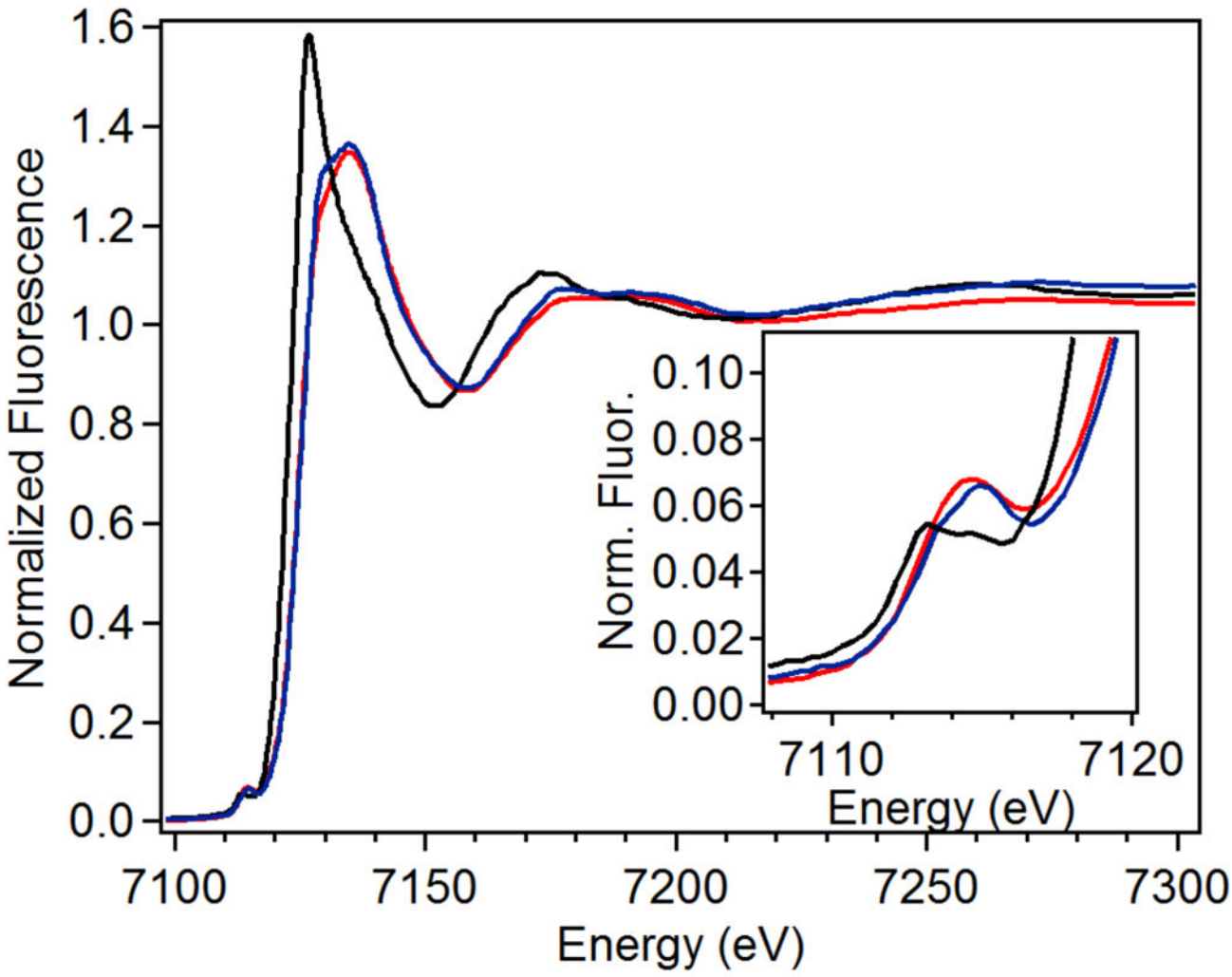

Figure 3.
XANES region for **CmlI^{R}** (solid black), **CmlI^{Ox}** (solid blue) and **CmlI^{P}** (solid red). Inset: Magnification of the pre-edge region.

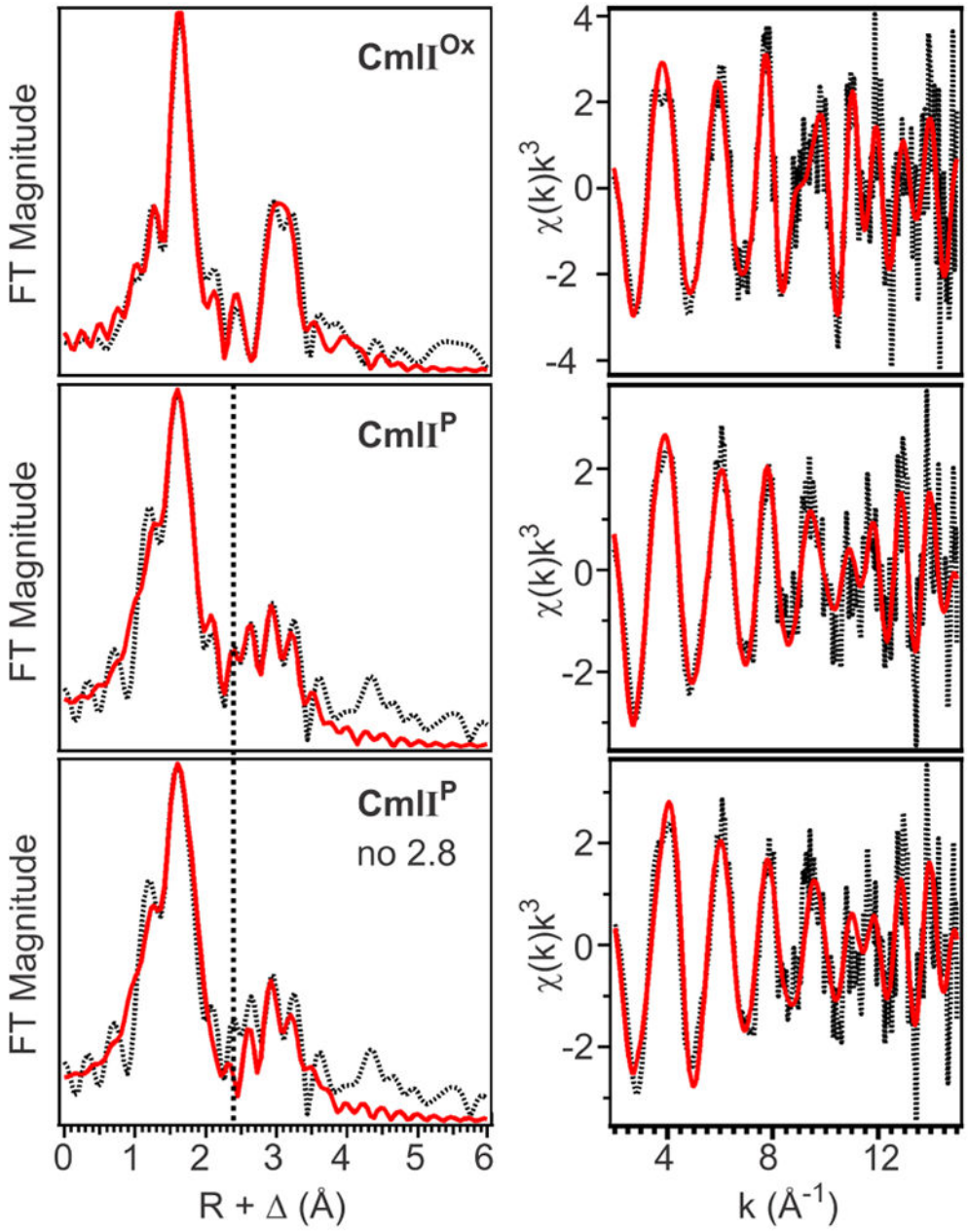

Figure 4.

Left Column: Fourier transforms of the EXAFS data (black dotted) with best fit (solid red) for **CmlI^{Ox}** (top; Table S2, fit 15), **CmlI^{P}** (middle; Table S3, fit 23) and **CmlI^{P}** without an Fe•••O scatterer at 2.82 Å (bottom; Table S3, fit 26), k range = 2 – 15 Å^{-1}. Vertical black dashed line shows the position of the FT feature associated with the 2.82-Å scatterer for **CmlI^{P}**. Right column: unfiltered EXAFS data (black dotted) with best fit (red solid) for **CmlI^{Ox}** (top; Table S2, fit 15), **CmlI^{P}** (middle; Table S3, fit 23) and **CmlI^{P}** without an Fe–O scatterer at 2.82 Å (bottom; Table S3, fit 26).

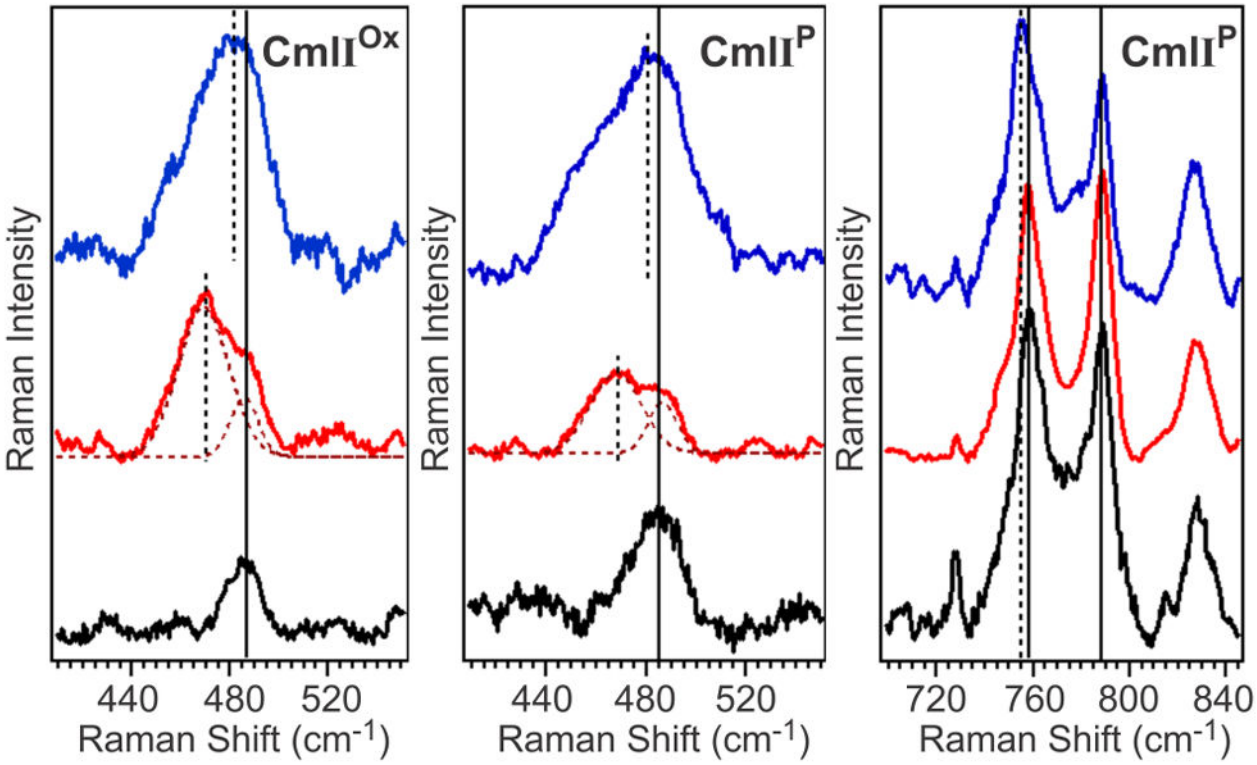

Figure 5.

Resonance Raman spectra of **CmII^{Ox}** (left), and **CmII^{P}** (middle, right) in $^{16}OH_2$ (black), $^{18}OH_2$ (red) and $^{16}OD_2$ (blue). The isotopic composition of water affects the Fe–O–Fe unit but not the peroxo moiety. λ_{ex} = 561 nm, Power = ~100 mW. All spectra were collected in solution at ~4 ºC. Protein concentration ~1 mM for each sample, 50 mM Bicine pH/pD = 9. $^{18}OH_2$ enrichment of the samples was ~60%.

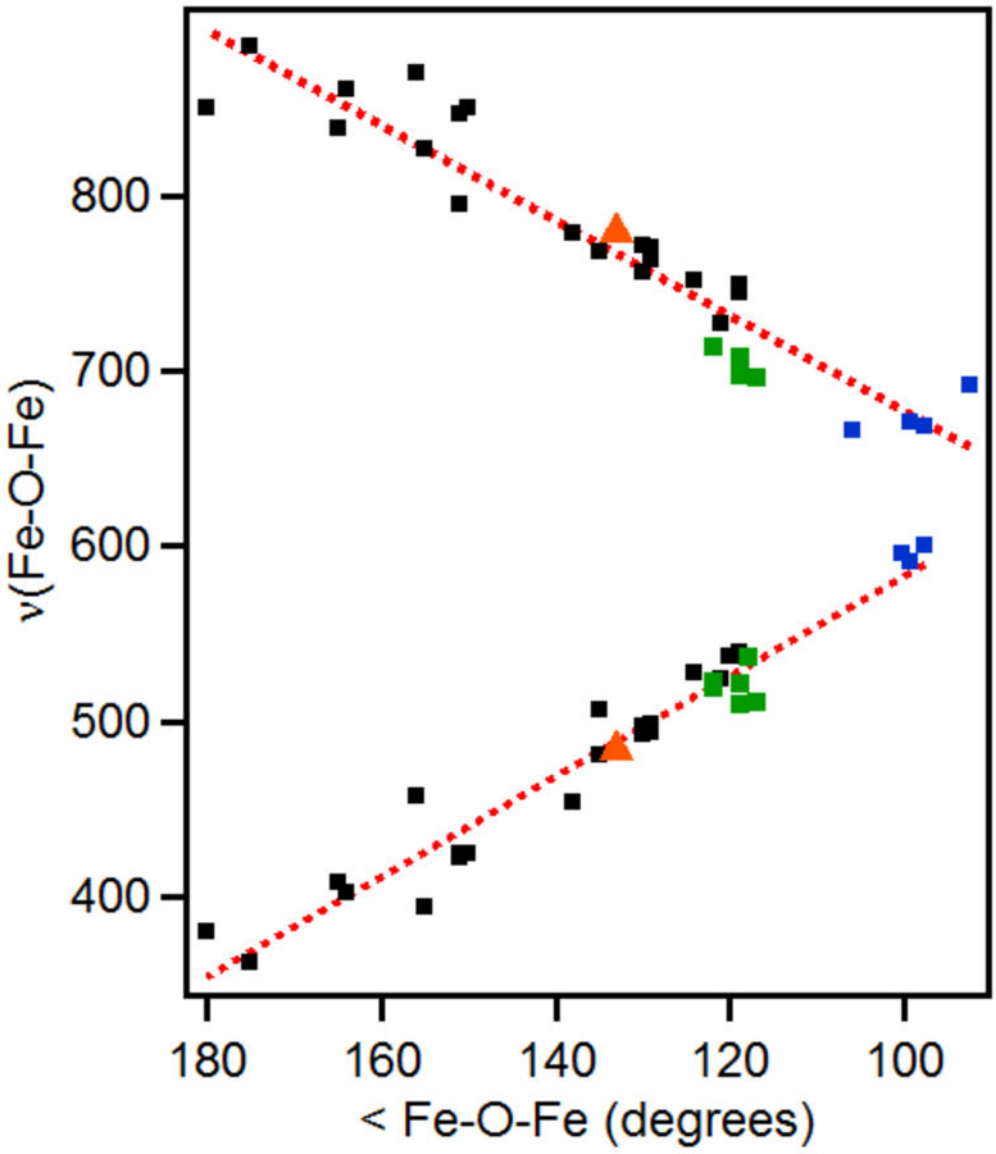

Figure 6.

Extended data set for the Sanders-Loehr correlation of ∠Fe–O–Fe and ν(Fe–O–Fe) in oxo-bridged diiron complexes. Data from the original study (black),[82] augmented by data for species with (μ-oxo)(μ-1,2-peroxo)diiron cores (green)[32, 60–62, 83] and species with bis(μ-oxo)diiron diamond cores (blue).[84–85] The data points corresponding to **CmlI^{P}** are shown as orange triangles. Red dotted lines represent the best linear fits of the data.

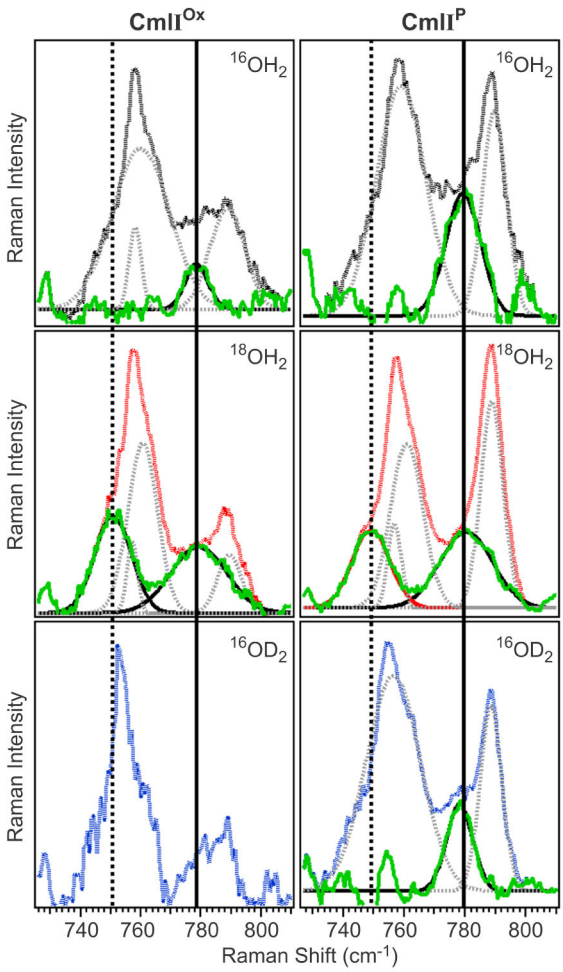

Figure 7.

Resonance Raman spectra of **CmlI^{Ox}** (left) and **CmlI^{P}** (right) in the 740–800-cm^{-1} region in $^{16}OH_2$ (top), $^{18}OH_2$ (middle) and $^{16}OD_2$ buffer (bottom). λ_{ex} = 561 nm, Power = ~100 mW. The experimental data (solid black, red lines) are fit with Gaussian functions to model the protein feature at ~760 cm^{-1} and the peroxo/protein peak at 789 cm^{-1}. These peaks are then subtracted from the experimental data (resulting green solid line). All spectra were collected in solution at ~4 ºC. Protein concentration ~1 mM for each sample, pH/pD = 9. $^{18}OH_2$ enrichment of the samples was ~60%.

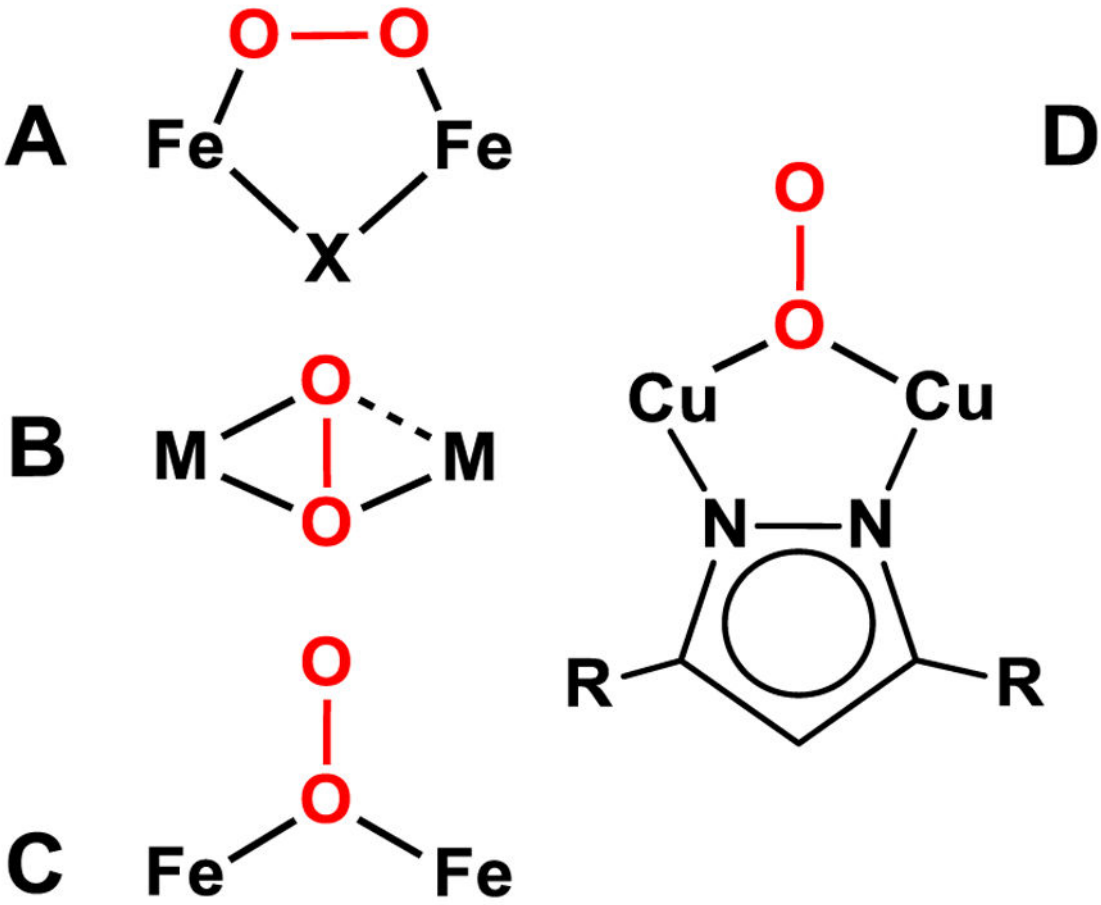

Figure 8.

O_2 binding modes for dimetal peroxide species relevant to the analysis of **CmlI^P**. X represents an additional bridging ligand, M represents a transition metal center, and R represents the remaining sections of the L_{et} ligand from **15**.

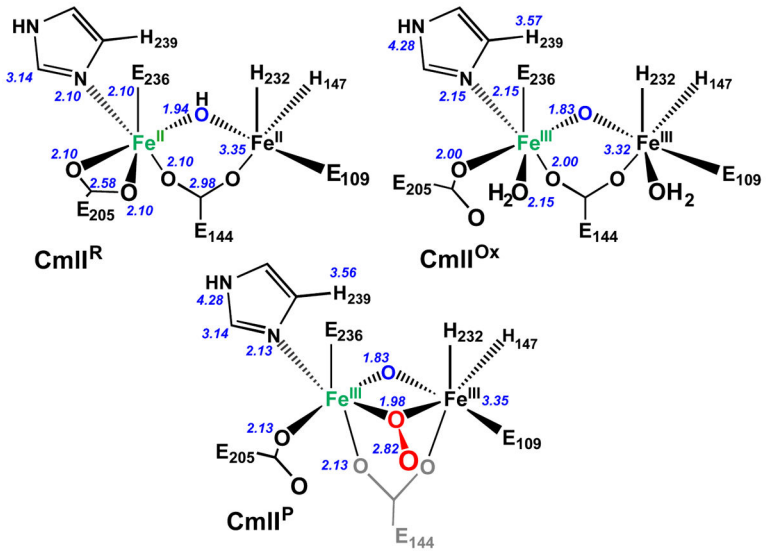

Figure 9.

Structural models of **CmII^{R}** (top left), **CmII^{Ox}** (top right) and **CmII^{P}** (bottom) as determined by EXAFS analysis. Numbers in italics represent the best fit scattering distances in angstroms. Fe1 atoms are colored green, and Fe2 atoms are colored black. The **CmII^{R}** structure has a Fe•••Fe distance of 3.35 Å and a calculated Fe– μ-OH–Fe angle of 119°, while **CmII^{Ox}** has an Fe•••Fe distance of 3.32 Å, and a calculated Fe– μ-O–Fe angle of 130°. **CmII^{P}** has an Fe•••Fe distance of 3.35 Å, and calculated Fe–μ-O–Fe and Fe–O_{peroxo}–Fe angles of 133° and 116°, respectively. The 2.82 Å values found for the Fe–O_{distal} distances require the O–O bond to be tilted out of the Fe–μ-O_{peroxo}–Fe plane.

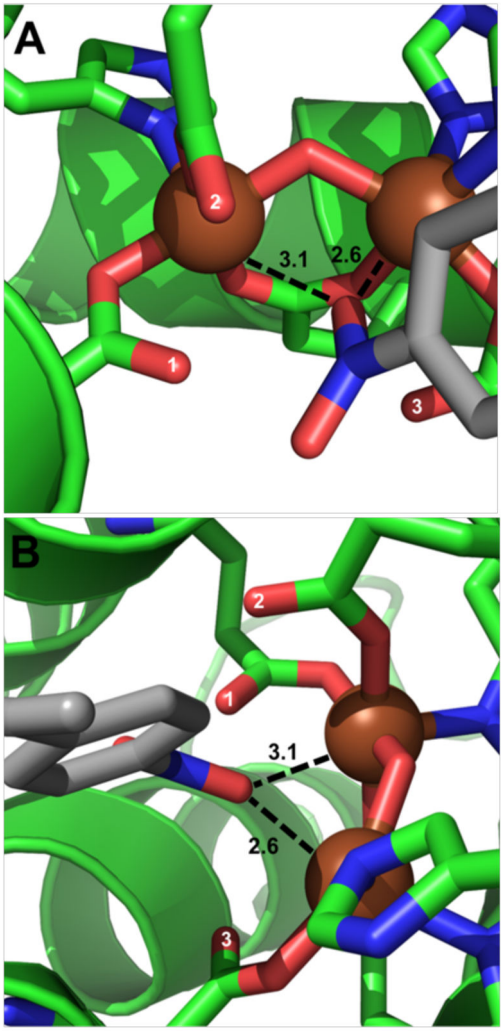

Figure 10.

Crystal structure of product-bound AurF (PDB code: 3CHT). Distances shown are in angstroms. Panel B is a 90º rotation of panel A. Carboxylate ligands that have oxygen atoms pointed toward the substrate channel are labeled 1 to 3. Carbon atoms from AurF are shown in green, oxygen atoms are in red, nitrogen atoms are in dark blue, iron atoms are represented as brown spheres and the carbon atoms of *para*-nitrobenzoic acid are shown as gray.

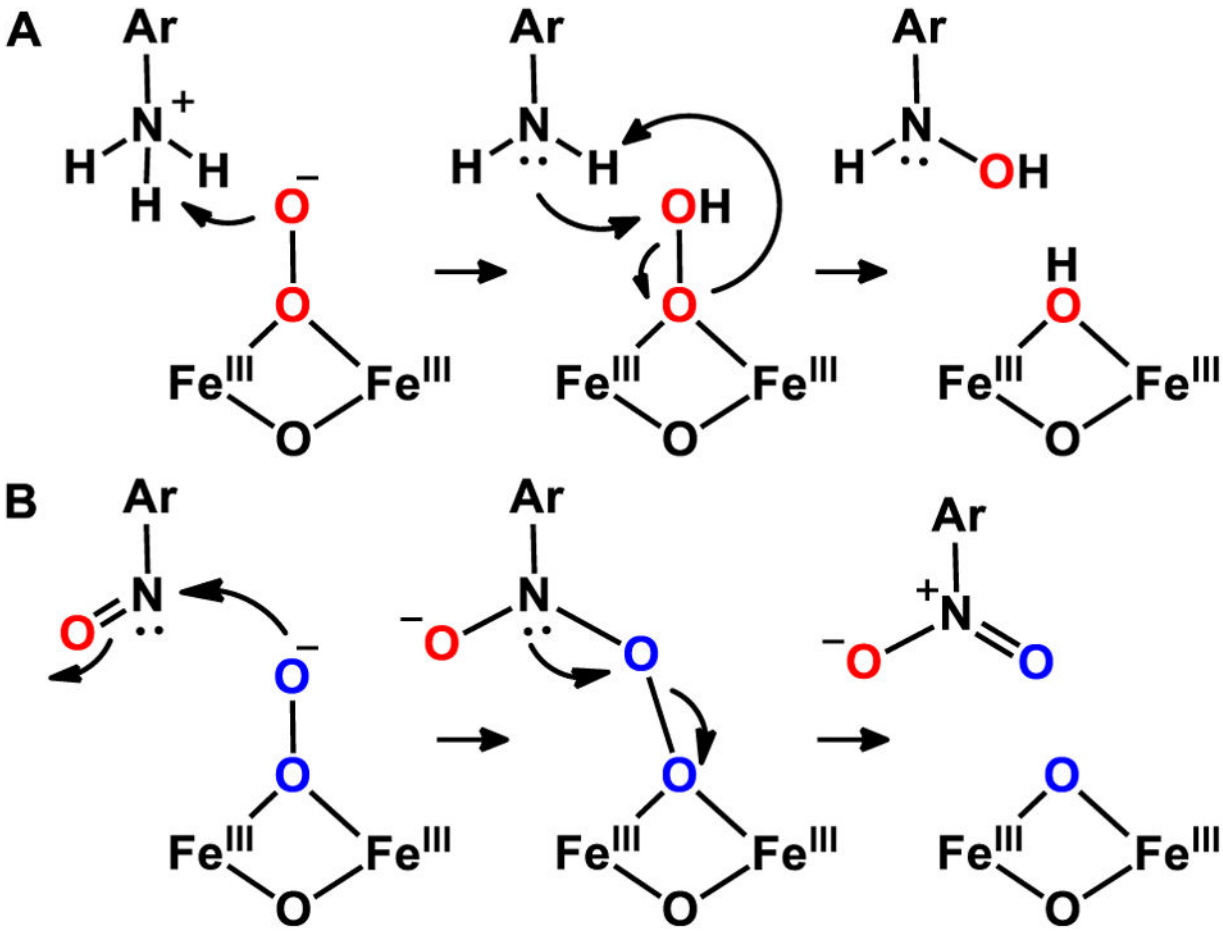

Figure 11.

Possible mechanisms for electrophilic (A) and nucleophilic (B) oxidation by **CmlI^{P}** along the native reaction pathway.

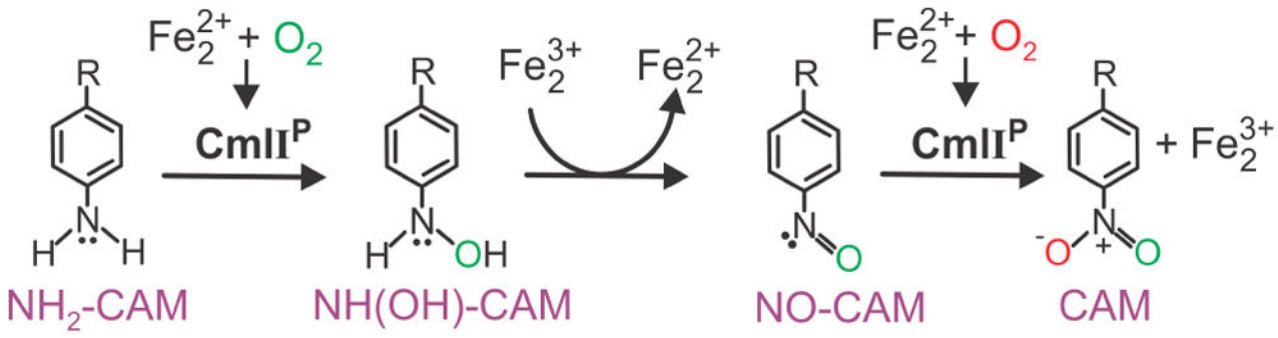

Scheme 1.
Proposed mechanism for the biosynthesis of chloramphenicol by CmlI.

Table 1

XANES analysis of CmlI Complexes and Related Species.

Species	K-edge (eV)	Pre-edge area (units)	Refs
CmlI^{R}	7122.1	8.4	This work
CmlA^{R}	7121.5	8.4	[58]
hDOHH^{R}	7122.7	8.6	[57]
CmlI^{Ox}	7124.1	14.5	This work
CmlA^{Ox}	7126.8	13.4	[59]
hDOHH^{Ox}	7125.2	7.8	[57]
CmlI^{P}	7124.9	19.2	This work
hDOHH ^{P}	7125.6	12.4	[57]

Table 2

Key distances for CmlI species obtained from EXAFS fits.[a]

	Fe–O			Fe-O/N			Fe••C/O			Fe•••Fe		
Fit	**N**	**R(Å)**	**$\sigma^2(10^{-3})$**	**N**	**R(Å)**	**$\sigma^2(10^{-3})$**	**N**	**R(Å)**	**$\sigma^2(10^{-3})$**	**N**	**R(Å)**	**$\sigma^2(10^{-3})$**
CmlI^{R}	1	1.94	5.35	5	2.10	5.02	1	2.58	1.35	1	3.35	9.90
CmlI^{Ox}	1	1.83	2.71	2	2.00	0.97				1	3.32	3.38
				3	2.15	1.73						
CmlI^{P}	1	1.83	4.05	2	1.98	2.09	1	2.82	1.50	1	3.35	4.47
				3	2.13	2.50						

[a]For complete fitting tables, see Tables S1 – S3.

Table 3

Select data points from the extended Sanders-Loehr correlation in Figure 6.

Species[a]	∠Fe-O-Fe (°)[b]	ν_s(Fe-O-Fe) (cm^{-1})[c]	ν_{as}(Fe-O-Fe) (cm^{-1})[c]	Refs
CmlI^P	133	485 (−18) [−4]	780 (−31) [−2]	This work
CmlI^{Ox}	130	487 (−18) [−7]	780 (−30) [−]	This work
CmlA	135	481 (−17)	-	59
oxyHr	*134*	486 (−14) [+4]	753 (−37)	87
metHrCN	137	512 (−14) [0]	782 (−28)	88
1	122	523 (−16)	714 (−14)	60
2	117	511 (−12)	696 (−30)	83
3	119	522 (−13)	708 (−32)	62
4	*130*	497 (−17)	772 (−37)	89
5	*124*	528 (−17)	751 (−30)	90
6	*99*	591 (−27)	671 (−31)	85
7	*93*	-	692 (−32)	84
8	106	-	666 (−32)	84

[a] Synthetic complexes in this column: **1** = $[(BnBQA)Fe^{III}_2(O)(O_2)(CH_3CN)_2]^{2+}$, BnBQA = *N*-benzyl-*N*,*N*-bis(2-quinolinylmethyl)amine; **2** = $[(6\text{-}Me_3TPA)_2Fe^{III}_2(O)(O_2)]^{2+}$, 6-Me$_3$TPA = tris(6-methyl-2-pyridylmethyl)amine; **3** = $[(BQPA)Fe^{III}_2(O)(O_2)]^{2+}$, BQPA = bis(2-quinolylmethyl)-2-pyridylmethylamine; **4** = $[(TPA)_2Fe^{III}_2(O)(OBz)]^{3+}$, TPA = tris(2-pyridylmethyl)amine, OBz = benzoate; **5** = $[(Tp)_2Fe^{III}_2(O)(OAc)_2]$, Tp = tris(1–pyrazolyl)borate; **6** = $[(6\text{-}Me_3TPA)_2Fe^{III}_2(O)(OH)]^{3+}$; **7** = $[(6\text{-}Me_3TPA)_2Fe^{III}_2(O)_2]^{2+}$; **8** = $[(5\text{-}Me_3TPA)_2Fe^{III}Fe^{IV}(O)_2]^{3+}$, 5-Me$_3$TPA = tris(5-methyl-2-pyridylmethyl)amine.

[b] Angles in italics come from X-ray diffraction studies, while the other angles are calculated from EXAFS data.

[c] Values in parenthesis indicate ^{18}O isotope shifts, while those in brackets are isotope shifts observed in D_2O buffer.

Table 4

Select structural metrics for **CmlI^{P}** and relevant synthetic peroxo complexes.

Species	Metal	Mode[a]	M•••M (Å)	M–O_p (Å)[b]	ν(O–O) (cm^{-1})
CmlI^{P}	Fe_2	C	3.35	1.98; 2.82	789
9	Fe_2	A	3.46	1.88; 2.91	900
10	Fe_2	A	3.40	1.88, 1.89; 2.86, 2.88	908
11	Fe_2	A	3.17	1.73; 2.97[c]	847
12	Fe, Cu	B	3.92	1.89, 1.92; 2.03, 2.66	790
13	Co_2	B	3.34	1.85, 1.92; 1.93, 2.76	839
14	Co_2	A	3.77	1.86; 2.70	866
15	Cu_2	D	3.53	1.99; 2.90, 3.00	860

[a] The mode listed in this column refers to the O_2 binding mode shown in Figure 8.

[b] In this column, the M–$O_{proximal}$ distance is listed first, followed by the M–O_{distal} distance.

[c] The μ-oxo and μ-1,2-peroxo atoms are disordered over two positions, each with 0.5 occupancy, so these values are not very reliable and represent the average from the crystal structure.